

## CANDIDATE TIDAL DWARF GALAXIES ASSOCIATED WITH THE STEPHAN'S QUINTET

C. MENDES DE OLIVEIRA <sup>1</sup>, H. PLANA <sup>2,3</sup>, P. AMRAM <sup>3</sup>, C. BALKOWSKI <sup>4</sup>, M. BOLTE <sup>5</sup>

*To appear in Astronomical Journal*

### ABSTRACT

We present kinematic and photometric evidence for the presence of seven candidate tidal dwarf galaxies in Stephan's quintet. The central regions of the two most probable parent galaxies, N7319 and N7318B, contain little or no gas whereas the intragroup medium, and particularly the optical tails that seem to be associated with N7318B are rich in cold and ionized gas.

Two tidal-dwarf candidates may be located at the edge of a tidal tail, one within a tail and for four others there is no obvious stellar/gaseous bridge between them and the parent galaxy. Two of the candidates are associated with HI clouds, one of which is, in addition, associated with a CO cloud. All seven regions have low continuum fluxes and high H $\alpha$  luminosity densities ( $F(\text{H}\alpha) = 1 - 60 \times 10^{-14} \text{ erg s}^{-1} \text{ cm}^{-2}$ ). Their magnitudes ( $M_B = -16.1$  to  $-12.6$ ), sizes ( $\sim 3.5 \text{ h}_{75}^{-1} \text{ kpc}$ ), colors (typically  $B - R = 0.7$ ) and gas velocity gradients ( $\sim 8 - 26 \text{ h}_{75} \text{ km s}^{-1} \text{ kpc}^{-1}$ ) are typical for tidal dwarf galaxies. In addition the ratios between their star formation rates determined from H $\alpha$  and from the B band luminosity are typical of other tidal dwarf galaxies. The masses of the tidal dwarf galaxies in Stephan's quintet range from  $\sim 2 \times 10^8$  to  $10^{10} M_{\odot}$  and the median value for their inferred mass-to-light ratios is  $7 M_{\odot}/L_{\odot}$ .

At least two of the systems may survive possible "fall-backs" or disruption by the parent galaxies and may already be or turn into self-gravitating dwarf galaxies, new members of the group.

*Subject headings:* galaxies: dwarf — galaxies: individual (NGC 7317, NGC 7318ab, NGC 7319, NGC 7320c) — galaxies: kinematics and dynamics — galaxies: interactions — galaxies: ISM — galaxies: intergalactic medium — cosmology: dark matter — instrumentation: interferometers — instrumentation: Fabry-Perot interferometer

### 1. INTRODUCTION

Optical and HI studies of interacting galaxies (e.g. Hibbard & van Gorkom 1996, Duc & Mirabel 1998) have shown that dwarf galaxies may be produced during galactic collisions. Duc & Mirabel (1998) have presented an especially convincing case of NGC 5291, where more than ten star-forming high-metallicity dwarf galaxies may have been formed in a recent merger. These newly formed tidal-dwarf galaxies may be good sites to study galaxy formation in the nearby universe.

Although the concept of the formation of self-gravitating objects in tidal tails is an old one, considered by Zwicky as early as in 1956, it is only recently that these objects have received more attention and have been searched for systematically. HI observations have so far been the principal means used in searches of tidal dwarf galaxies since these are usually gas-rich systems. HI maps can reach large radii but have the disadvantage of being (mostly) of too poor spatial resolution for a direct investigation of the velocity field of the spatially-small and low-velocity-dispersion objects (typically 5-20 arcsec in extent, and velocity gradients of  $2 - 20 \text{ km s}^{-1} \text{ arcsec}^{-1}$ ; Duc, 1995). The study of the kinematics of the ionized gas of a galaxy, when it is present, with high spatial and spectral resolution velocity maps, can alternatively provide a useful tool to probe the nature of the candidate dwarf galaxies at small scales,

complementing the lower-resolution radio studies.

This paper presents new data on the kinematics of the ionized gas for seven star-forming tidal dwarf galaxy candidates and many other giant HII regions of Stephan's quintet. Combining Fabry Perot H $\alpha$  maps with deep B and R images, we study the photometric and kinematic properties of 23 emission-line regions of the group.

Stephan's Quintet (Arp 319, VV288, HCG 92) has been the subject of studies in x-rays, radio continuum, HI and H $\alpha$ . Most of its gaseous material is not concentrated around the bright galaxies but in the intragroup medium, suggesting that collisions among the group members may have taken place. Arp (1973) was the first to obtain an H $\alpha$  image of the group and to identify HII regions around galaxies N7318A,B, N7319 and N7320. As part of an imaging survey of compact groups, in the R band, Hunsberger et al. (1996) identified 27 tidal dwarf galaxy candidates possibly associated with N7318A,B and N7319. One of these regions was observed by Xu et al. (1999) to be a bright infrared source, when observed with the ISO satellite (their source A). Xu et al. (1999) also presented H $\alpha$  + [NII] images of the group highlighting the spatial overlap of the two emission clouds of ionized gas in the intragroup medium centered around  $5700 \text{ km s}^{-1}$  and  $6700 \text{ km s}^{-1}$ . A similar result was found by Plana et al. (1999) based on Fabry-Perot H $\alpha$  maps.

An interesting possible scenario for the interaction his-

<sup>1</sup> Instituto Astronômico e Geofísico (IAG), Av Miguel Stefano 4200 CEP: 04301-904 São Paulo, Brazil

<sup>2</sup> Observatorio Astronomico Nacional, UNAM, Apartado Postal 877, 22800, Ensenada, BC, México

<sup>3</sup> Laboratoire d'Astrophysique de Marseille, Observatoire de Marseille, 2 Place Leverrier, 13248 Marseille Cedex 04 France

<sup>4</sup> Observatoire de Paris, DAEC and UMR 8631, CNRS and Université Paris 7, 5 Place Jules Janssen, F-92195 Meudon Cedex, France

<sup>5</sup> Lick Observatory, Board of Studies in Astronomy and Astrophysics, University of California, Santa Cruz, California 95064

tory of Stephan’s quintet has been put forward by Shostak et al. (1984) and refined by Moles et al. (1997, 1998). The scenario is based on the analysis of optical images of the quintet, spectroscopy of a number of systems (Moles et al. 1998) and HI maps which show three velocity components associated with the group, at  $\sim 5700 \text{ km s}^{-1}$ ,  $6000 \text{ km s}^{-1}$  and  $6700 \text{ km s}^{-1}$  (Balkowski et al. 1973, Allen & Sullivan 1980, Shostak et al. 1984). In their scenario, one or more major collisions occurred between N7320C and N7319 (at velocities  $\sim 6000 \text{ km s}^{-1}$  and  $\sim 6700 \text{ km s}^{-1}$  respectively), which may have resulted in the removal of the HI gas from the inner parts of N7319. More recently, Stephan’s quintet would have received a new member, N7318B (it has a radial velocity of  $5774 \text{ km s}^{-1}$  while the other core-group members, N7317, N7318A and N7319, have a mean velocity of  $6664 \text{ km s}^{-1}$ , Hickson et al. 1992). N7318B would be entering the group for the first time and it would be colliding with the intragroup medium (Moles et al. 1997). We identify a number of possible tidal dwarf galaxy candidates most probably formed as a result of the ongoing collision that involves N7318B. Only one of the candidates studied here may be associated with the collision N7320C–N7319 and hence the HI cloud removed from the center of N7319. An alternative possibility is that the latter originated from N7318A (see Sections 4.7 and 4.8).

All the regions we measure in this work have been previously identified as HII regions by Arp (1973). A number of them have also been listed by Hunsberger et al. (1996) as tidal dwarf galaxy candidates and Gallagher et al. (2000, using HST images) as massive cluster candidates. However, these studies did not have velocity information. Radial velocity information for some of the regions is summarized in Table 1 of Plana et al. (1999). Determination of the velocity gradients within the regions is the main contribution of the present work.

The organization of this paper is as follows. Section 2 describes the observations and reduction procedure. In Section 3, we present the new photometric and kinematic results. In Section 4, we discuss the results and section 5 summarizes the paper. Throughout this paper  $h_{75}$  is the Hubble constant in units of  $H_0 = 75 \text{ km s}^{-1} \text{ Mpc}^{-1}$ . We assume that all the regions are at the same distance, and the differences in  $cz$  are just kinematical. For the figures and the determination of the star-formation rates we assumed a distance to the group of 80 Mpc, for an average velocity of  $6000 \text{ km s}^{-1}$  and a Hubble constant of  $75 \text{ km s}^{-1} \text{ Mpc}^{-2}$ .

## 2. OBSERVATIONS AND DATA REDUCTION

### 2.1. Fabry Perot data

The observations were carried out with a scanning Fabry-Perot instrument mounted on the Canada-France-Hawaii 3.6m telescope (CFHT) and the Russian SAO 6m telescopes. The observations and characteristics of the setups are summarized in Table 1. During the CFHT run we mostly detected sources with radial velocities  $V_R \sim 5700 \text{ km s}^{-1}$ , since we used a narrow-band filter that cut the higher velocities. We, therefore, did not detect the  $6700 \text{ km s}^{-1}$  velocity component of the group. The filter used during the observations at the Russian SAO 6m telescope allowed the detection of a much broader range of wavelengths and both velocity components were detected.

However, the data are of much lower signal-to-noise and spectral and spatial resolution than the CFHT data.

Reduction of the data was performed using the CIGALE/ADHOC software (<http://www-obs.cnrsmrs.fr/adhoc/adhoc.html>). The data reduction procedure has been extensively described in Amram et al. (1995, 1996), Plana et al. (1998) and references therein.

Wavelength calibrations were obtained by scanning the narrow Ne 6599 Å line during the observations. The relative velocities with respect to the systemic velocities are very accurate, with an error of a fraction of a channel width ( $< 3 \text{ km s}^{-1}$ ) over the whole field.

The signal measured along the scanning sequence was separated into two parts: (1) a constant level produced by the continuum light in a narrow passband around H $\alpha$  (continuum map), and (2) a varying part produced by the H $\alpha$  line (monochromatic map). The continuum level was taken to be the mean of the three faintest channels. The monochromatic map was obtained by integrating the monochromatic profile in each pixel.

The CFHT data were roughly calibrated in flux using a common galaxy also observed in a previous run when a flux calibrator was observed (Amram et al. 1998). We estimate an error of 30% in the flux calibration. The H $\alpha$  profiles were measured to a minimum flux density of  $4.9 \times 10^{-17} \text{ erg s}^{-1} \text{ cm}^{-2} \text{ arcsec}^{-2}$ . We were not able to flux calibrate the data obtained at the SAO 6m telescope for lack of calibrators.

### 2.2. Imaging

Images of Stephan’s quintet in B (5 x 900s) and R (6 x 350s) were obtained with the CFHT and the Subarcsec Imaging instrument. The values of seeing on the final images were 0.8 and 0.6 arcsec respectively.

Preprocessing of all frames through flat-fielding was carried out using IRAF tasks. The individual frames were registered and combined with a clipping scheme that eliminated one lowest and one highest pixel values in each registered stack to exclude cosmic rays, hot pixels and low pixels.

The program SExtractor (Bertin & Arnouts 1996) was used to obtain the photometry of all objects in the B and R images with a sky “meshsize” of 128 pix. “Automatic-aperture magnitudes” were obtained, which give total magnitudes for the objects (based on the Kron’s, 1980, first-moment algorithm).

Calibration to the standard system for the B and R band observations was done via observations of standard stars from the list of Landolt (1992) and updated magnitudes for the KPNO consortium fields in M92 and NGC 7006. The transformations from instrumental to standard systems were made using the following:  $R = r + 0.015(B - R) + 31.37$  and  $B = b + 0.047(B - R) + 31.27$ . The final combined images of H92 can be obtained upon request. A B–R map was obtained after the images were calibrated and their seeing profiles were matched (shown in Fig. 1a).

## 3. RESULTS

### 3.1. Magnitudes and colors of the emission-line regions

The H $\alpha$  contours superimposed on the B–R image of Stephan’s quintet is shown in Fig. 1a. The 23 emitting

TABLE 1  
JOURNAL OF PEROT-FABRY OBSERVATIONS

HCG 92 or Stephan’s quintet			
Observations	Telescope	CFHT 3.6m	SAO 6m
	Equipment	MOS/FP @ Cassegrain	CIGALE @ Primary
	Date	August, 23th 1996	August, 5th 1991
	Seeing	< 1”	~ 1.2”
Interference Filter	Central Wavelength	6697 Å <sup>1</sup>	6726 Å <sup>2</sup>
	FWHM	17 Å <sup>1</sup>	50 Å <sup>2</sup>
	Transmission (Maximum)	0.7 <sup>1</sup>	0.55 <sup>2</sup>
Calibration	Neon Comparison light	λ 6598.95 Å	λ 6598.95 Å
Perot–Fabry	Interference Order	1162 @ 6562.78 Å	796 @ 6562.78 Å
	Free Spectral Range at Hα	265 km s <sup>-1</sup>	380 km s <sup>-1</sup>
	Finesse at Hα	12	12
	Spectral resolution at Hα	27344 at the sample step	18750
Sampling	Number of Scanning Steps	24	24
	Sampling Step	0.24 Å (11 km s <sup>-1</sup> )	0.35 Å (16 km s <sup>-1</sup> )
	Total Field	440” × 440” (512 × 512 px <sup>2</sup> )	170” × 170” (256 × 256 px <sup>2</sup> )
	Pixel Size	0.86”	0.67”
Detector		STIS 2 CCD	IPCS
Exposures times	Total exposure time	1.2 hours	0.8 hour
	Each scanning exposure time	180 s	20 s per channel
	Total exposure time per channel	180 s	120 s

<sup>1</sup>For a mean beam inclination of 2.7°

<sup>2</sup>For a mean beam inclination of 5.3°

regions detected by Plana et al. (1999) are marked. Dark is blue and white is red. The letters “L” and “H” are used to identify the systems for which we have an unambiguous determination of their radial velocities. The ones marked with “L” belong to the low-velocity system associated with N7318B, with velocities of 5700–6000 km s<sup>-1</sup> and the only system marked with “H”, region 6, is the high-velocity system probably associated with N7319, at a velocity of ~ 6700 km s<sup>-1</sup>.

In Fig. 1b the corresponding R image of the group (after subtraction of a heavily smoothed sky) is shown. The optical blobs corresponding to the Hα emitting regions are marked in this figure (e.g. regions 1A and 1B correspond to the B and R counterparts of region 1 in Hα, see Fig. 1a). All regions detected in Hα have counterparts on the B and R image. Region 17 is faint, it is affected by dust, and it is too close to the galaxy N7318A. Although it is not evident given the contrast of Fig. 1b, it does have a counterpart on the B and R images.

The B–R image of the group shown in Fig. 1a reveals some interesting features. The galaxy N7319 may contain several dust spots (white regions in the figure, which are those with the reddest values of B–R), particularly the one to the north of the galaxy corresponds to strong CO emission (Gao & Xu 2000). We also note that the center of galaxy N7318A has a dust lane with a very peculiar shape, suggesting that this galaxy may have taken part in the interaction history of the group (not contemplated in the scenario described by Moles et al. 1997). The complicated dust lane structure of N7318A is much more impres-

sive in the HST image of the group obtained by Charlton et al. (2000). Further evidence that galaxy N7318A may be in interaction is given by Fig. 1c, which is discussed in Section 4.7.

Table 2 shows the main photometric parameters for all the 23 Hα-emitting regions shown in Figs. 1a and 1b (with exception of a few entries for region 17, for the reason explained previously). Total B magnitudes (“automatic-aperture magnitudes” given by SExtractor) and B–R colors are listed in columns 2 and 3. When one Hα region corresponds to more than one identification on the B and R images we list the apparent B magnitudes of the different blobs in a single entry, separated by slashes (magnitudes and colors are corrected for Galactic extinction only). The B–R color was measured inside an aperture of 1.0 arcsec radius centered on each blob. The total absolute magnitudes given in column 3 correspond to the sums of the individual luminosities (e.g. the absolute magnitude for region 8, see Fig. 1a, corresponds to the sum of regions 8A, 8B and 8C, see Fig. 1b). The ID’s marked with a “c” on Table 2 correspond to the candidate tidal dwarf galaxies (see section 3.3). The magnitude and color of region 14A is contaminated by light from a red background galaxy that overlaps with this region. There is an object to the northwest of region 2 which also seems to be a background object, given its red color.

We measure a very low continuum level (on the Fabry-Perot map) for several of the Hα-emitting regions. Since we were not able to perform calibration in flux of the continuum map (for lack of calibrators), we determined the

TABLE 2  
 PROPERTIES OF THE STAR-FORMING REGIONS OF STEPHAN'S QUINTET

ID	B (mag)	$M_B$ (mag)	$(B-R)_0$ (mag)	Cont. (%)	$F(H\alpha)^a$ $\times 10^{-14}$	$SFR(H\alpha)^b$	$SFR(L_B)^b$ $\times 10^{-3}$	$a \times b$ (arcsec)
1	20.7/21.9	-14.2	0.76	3.1	1.5	0.23	2.2	9.0 x 8.4
2 <sup>c</sup>	20.6	-14.0	0.53	2.3	28.7	4.26	12.2	34 x 17
3 <sup>c</sup>	20.3/20.9	-14.7	0.55	3.3	–	–		
4 <sup>c</sup>	21.2	-13.4	0.67	3.2	–	–		
5 <sup>c</sup>	19.6/20.7	-15.3	0.47	3.9	–	–		
6 <sup>c</sup>	19.5	-15.0	1.32	3.6	–	–	4.5	16.0 x 13.0
7	21.5	-13.0	0.75	3.2	0.3	0.04	0.7	2.6 x 3.4
8*	21.4/22.3/21.2	-14.2	0.79	3.0	2.5	0.38	2.2	13.7 x 7.5
9	23.2	-11.4	1.00	–	2.5	0.38	0.2	7.4 x 4.6
10	20.1	-14.5	0.92	6.3	0.7	0.09	2.9	3.1 x 3.1
11	20.8	-13.7	0.58	4.8	0.7	0.09	1.4	4.7 x 3.1
12	19.6	-4.9	0.43	4.6	0.7	0.10	4.1	8.3 x 4.8
13	21.5	-13.0	0.77	–	2.2	0.32	0.7	8.6 x 5.6
14 <sup>d</sup>	19.3/21.2	-15.4	0.94	6.3	8.1	1.20	6.5	9.2 x 6.7
15	20.8/20.4	-14.7	1.00	4.7	9.6	1.42	3.4	10.8 x 9.3
16	21.1/21.6/22.0/21.5	-14.3	0.86	5.4	3.2	0.46	2.4	3.3 x 3.1
17	–	–	–	–	2.7	0.40	–	5.4 x 3.5
18	19.7/21.0	-15.1	0.56	4.0	13.4	2.00	4.9	11.9 x 9.0
19	20.3/21.5	-14.6	0.71	2.9	9.0	1.35	3.1	15.0 x 7.2
20 <sup>c</sup>	21.9	-12.6	0.76	0.3	3.0	0.45	0.5	10.5 x 8.0
21 <sup>c</sup>	20.1	-14.4	0.34	2.0	4.9	0.73	2.6	11.3 x 10.5
22 <sup>c</sup>	21.0/21.7/22.2	-14.2	0.42	1.0	4.2	0.63	2.2	11.8 x 9.7
23 <sup>c</sup>	21.5	-13.0	0.63	0.2	1.3	0.20	0.7	8.2 x 8.7

<sup>a</sup>the units are  $\text{erg s}^{-1} \text{cm}^{-2}$

<sup>b</sup>the units are  $M_\odot \text{yr}^{-1} L_\odot^{-1}$

<sup>c</sup>objects classified as tidal dwarf galaxies

<sup>d</sup>the magnitude and color of this region are contaminated by light from a red background galaxy

ratio of the total flux contained in each blob to the flux within an arbitrary aperture of radius  $1.8''$  centered on galaxy N7318B. This fraction (in percentage) is shown in column 5 of Table 2. This procedure is intended to show, in a relative way, which regions are the ones with brightest and faintest continuum emission. The regions with the lowest fluxes are regions 20 and 23. They have  $\sim 10$  times less flux in the continuum than the median for the remaining regions. Regions 9, 13 and 17 could not be measured due to contamination from the bright galaxies N7318A,B.

We show color gradients for each emission-line blob in Fig. 2. The  $(B-R)_0$  (corrected for galactic extinction) profiles in general become bluer toward each HII region, despite the fact that the R-band flux is contaminated by the  $H\alpha$ -line emission. We can see from column 4 of Table 2 that all but one emitting region detected in  $H\alpha$  are blue (the median value of the color is 0.7). The exception is region 6, with a B-R color of 1.3.

### 3.2. *The kinematics and the nature of the emission-line regions*

Plana et al. (1999) detected 23  $H\alpha$  emitting regions around the N7318A/B system. For seven of them (six systems and one complex with four regions) a velocity field is derived and shown in Figs. 3a to 3g. These correspond to the objects which show rotation. The velocity fields were used to derive the rotation curves shown in Fig. 4. In all cases the velocities were measured within  $\pm 35^\circ$  of the major axis in the plane of the sky, except for regions 2–5 and 6, where a cone of  $\pm 40^\circ$  was used instead. The rotation curves were obtained using the position angle and inclination listed in columns 2 and 3 of Table 3. The position angle of the major axis (given in column 2) is taken to be the axis of symmetry of the main kinematic body of each galaxy. The center of the velocity field is whenever possible chosen to be a point along the major axis which makes the rotation curve symmetric, with similar amplitudes for the receding and approaching sides (this is, however, not always possible, e.g. region 6). The values of inclination with respect to the plane of the sky (given in column 3) are determined from the velocity fields of the candidates. Specifically we used a least square's fit program which gives the best value for the inclination fixing the position angle, the central systemic velocity and the kinematic center and by fitting a classical rotation velocity model for data points inside crowns at increasingly growing distances from the center.

In the top-left panels of Figs. 3a–g we show the  $H\alpha$  contours determined from the CFHT Fabry-Perot maps, superimposed on the deep B-band image of the galaxy (see also Plana et al. 1999). For region 6 the  $H\alpha$  map is derived from the SAO 6m data (since its velocity was outside the filter range for the CFHT observations). The lower-left panels show the continuum-subtracted emission-line profiles. These have been smoothed spectrally by a gaussian function having a FWHM of three channels (or  $35 \text{ km s}^{-1}$ ) and spatially ( $3 \times 3$  pixels), except for Fig. 3a (see below). Each pixel represents  $0.86''$  on the sky. Although the pixel size for the image of region 6 was originally  $0.67''$ , it was degraded to  $0.86''$  to match the CFHT data. In the right panels we show the velocity fields of the galaxies superimposed on the corresponding monochromatic  $H\alpha$  images.

We mark the absolute value for each isovelocity for regions 2–5, 6 and 21, but for regions 8, 20, 22 and 23, only relative velocities are marked, since we do not know the systemic velocities of these regions.

We classify systems 2–5, 6, 8, 20, 21, 22 and 23 as tidal dwarf galaxy candidates on the basis of the clear signature of rotation, above a cut-off value of  $8.0 \text{ h}_{75} \text{ km s}^{-1} \text{ kpc}^{-1}$ ). Examples of non-rotating structures, possible associations of giant HII regions, are regions 9, 10, 11, 14, 15, 18 and 19.

We see continuous profiles between regions 9 to 11 (the data have  $S/N > 20$  in between the emission blobs) showing that these are connected. These regions are most probably attached to the southern tail of N7318B. No velocity gradients are detected within them. Regions 14 and 15 are attached to one or more tidal tails (these regions correspond to double velocity components, Plana et al. 1999). Even if these complexes have  $H\alpha$  fluxes, sizes and colors consistent with their being tidal dwarf galaxies (like the ones studied by Duc 1995), we detect no velocity gradient within the objects. In the same way, regions 18 and 19 also show bright  $H\alpha$  emission with no velocity gradients. These are very close to N7318A but, as indicated by their radial velocities ( $\sim 5700 \text{ km s}^{-1}$ , Plana et al. 1999), they may belong to N7318B. Regions 18 and 19 do not have any obvious contact to a tidal arm.

Region 1 is isolated. We detected no velocity gradient within the region but the  $S/N$  of the data may be too low to allow a gradient measurement.

We summarize below the properties of each object that we classify as candidate tidal dwarf galaxies.

### 3.3. *Properties of the candidate tidal dwarf galaxies*

**Regions 2–5:** The complex formed by regions 2–5 has a radial velocity of  $6020 \text{ km s}^{-1}$  (velocity obtained by Moles et al. 1998 for region 2) and it shows an  $H\alpha$  diameter (full width at zero intensity) of  $\sim 34''$  (corresponding to a radius of  $R=6.5 \text{ h}_{75}^{-1} \text{ kpc}$ ). In order to increase the  $S/N$  ratio we performed a spatial smoothing of  $3 \times 3$  pixels in the center and  $5 \times 5$  pixels outside the inner region. Since this complex is large, smoothing does not affect the results. We can see on the lower-left panel of Fig. 3a that the complex formed by regions 2–5 is connected by continuous velocity profiles. Although with a much lower  $S/N$ , the effect is also measurable in the unbinned data. This suggested to us that these regions may form one system, perhaps within a tidal tail. Fig. 4a shows the corresponding rotation curve. The approaching and receding sides of the rotation curve differ in shape and amplitude. The curve is increasing regularly, reaching the average maximum velocity of  $50 \text{ km s}^{-1}$ . As the monochromatic map shows, we have at least four emitting regions and therefore the velocity field and rotation curve may be averages of internal motions of these various regions. This could explain, at least partially, the disturbances of the velocity field. The R image in Fig. 1b shows at least six bright condensations. The system as a whole has no defined center. The conditions needed for the complex of regions 2–5 to become an independent galaxy are discussed in Sections 4.1 and 4.6. We conclude that there is little chance that this region will survive as a single object. It could, however, form several condensations that could then be stable. We point out that there is an HI

cloud encompassing the region with velocity similar to the optical velocity measured from the H $\alpha$  emission ( $\sim 6000$  km s $^{-1}$ , Williams et al. 1999).

**Region 6:** Region 6 has a radial velocity of 6680 km s $^{-1}$  (Moles et al. 1998). It shows a disturbed and fairly extended velocity curve out to a radius of  $R \sim 3.5 h_{75}^{-1}$  kpc. The profiles shown in the lower-left panel of Fig. 3b indicate a larger velocity dispersion (i.e. they have larger widths) than for the other regions ( $\sim 115$  km s $^{-1}$  compared to 80 km s $^{-1}$  for the others). A larger dispersion is expected when there is, for example, a second component blended with the main velocity component. However, in the case of region 6, the components are not resolved and any attempt to decompose them would be arbitrary. As can be seen in Fig. 3b, some of the profiles do show double peaks but no consistent solution for a moving second component could be found, perhaps due to low S/N. The rotation curve presented in Fig. 4b is peculiar. There is complete disagreement between the amplitudes of the receding and the approaching sides. The approaching side has approximately constant velocity at  $\sim 10$  km s $^{-1}$  while for the receding side the velocity reaches 90 km s $^{-1}$ . The maximum rotational velocity listed in Table 4 is taken to be the average between both sides. The mass estimate obtained from this number is therefore very uncertain. Williams et al. (1999) have detected an HI cloud at the position of Region 6 with similar velocity to that measured from the H $\alpha$  emission ( $\sim 6700$  km s $^{-1}$ ). It was also detected in CO by Gao & Xu (2000). In addition, this region was detected with ISO by Xu et al. (1999) and it was found to be a very bright source in the infrared. This could therefore be a peculiar object, given its infrared luminosity and its disturbed rotation curve.

**Region 8:** It shows an extent of  $R \sim 4.5 h_{75}^{-1}$  kpc. The velocity field is quite regular. Fig. 4c shows the rotation curve rising up to an average maximum velocity of 115 km s $^{-1}$  in 12 arcsec ( $\sim 4.5 h_{75}^{-1}$  kpc). This is the largest maximum rotational velocity we detect for a candidate tidal dwarf galaxy. Interestingly enough, this is the only tidal dwarf galaxy that seems to be embedded in a tidal tail and it is the one closest to the parent galaxy. Nonetheless the very high velocity gradient measured along a very short path and the optical condensations coincident with the emission-line region motivated us to list this as a possible candidate.

**Region 20:** It has an extent of  $R \sim 3.2 h_{75}^{-1}$  kpc. As the profiles of Fig. 3d show, the emission is centrally concentrated. The rotation curve presented in Fig. 4d is regular except outside a radius of  $2 h_{75}^{-1}$  kpc, where we can see a discrepancy between the approaching and the receding sides. The average maximum velocity is 30 km s $^{-1}$ . The R image in Fig. 1b shows a single center and no bridge to the parent galaxy (possibly N7318B).

**Region 21:** It has an extent of  $R \sim 3.5 h_{75}^{-1}$  kpc. The velocity field (Fig. 3e) does not show perturbed isovelocities, but the position angle changes along the radius. The rotation curve, shown in Fig. 4e, is derived along a mean position angle of the major axis of  $\sim 80^\circ$ . The approaching side of the rotation curve has a normal behavior, with velocities increasing up to 65 km s $^{-1}$ . For the receding side, due to the position angle change, the velocities are scattered beyond  $2 h_{75}^{-1}$  kpc. The R image in Fig. 1b

shows two condensations, the one most to the west being the brightest.

**Region 22:** It shows an extent of  $R \sim 3 h_{75}^{-1}$  kpc. The velocity field is disturbed. A second component may also be present in this case, as suggested by the profiles of Fig. 3f. We were not able, however, to do a satisfactory decomposition of the two components. The rotation curve, shown in Fig. 4f, presents a strong rise in the first 2", a decrease in velocities after that and then a new increase around  $R \sim 6''$ . The error bars are very large for radii beyond 6" indicating a higher scatter in the velocities. Three condensations are seen in the optical image, the ones most to the east being the brightest. It is interesting to note that the blueshifted isovelocities of region 22 point towards the blueshifted isovelocities of region 21. This suggests the velocity gradients measured are probably intrinsic to the regions and are not larger scale motions within a possible faint tidal tail that joins the regions.

**Region 23:** It has an extent of  $R \sim 2 h_{75}^{-1}$  kpc. The velocity field (Fig. 3g) does not show disturbed isovelocities, but the rotation curve (Fig. 4g) shows that the velocities for the approaching side increase in the first 2" and then decline while the velocities for the receding side increase with radii. The receding and the approaching sides are therefore not in agreement.

The rotation curves for four of the galaxies rise linearly with radius, without reaching a significant plateau. For two dwarf galaxy candidates, regions 22 and 23, the shape of the curve is disturbed. For region 6, the shapes of the approaching and receding sides are very different.

The rotation curves presented here can be compared with those for other tidal dwarf galaxies and blue compact galaxies. This is done in Section 4.2.

### 3.4. H $\alpha$ luminosities and SFR's

Table 2 gives H $\alpha$  fluxes for each emitting region, derived from the calibrated monochromatic map, measured above a threshold of  $4.9 \times 10^{-17}$  erg s $^{-1}$  cm $^{-2}$  arcsec $^{-2}$ , within apertures of diameters given in column 9 (defined as the diameter of the aperture of zero intensity). For region 6 no flux is listed given that the data for this region is uncalibrated (see Section 2.1).

The current star formation rate can be derived from the formula  $\text{SFR}(H_\alpha) = 7.5 \times 10^{-8} L_{H_\alpha} (M_\odot \text{yr}^{-1} L_\odot^{-1})$ . This formula is valid for 0.1 – 100  $M_\odot$  (Hunter & Gallagher 1986). The H $\alpha$  fluxes given in column 6 of Table 2 were transformed to luminosities for use in the formula above integrating over the sphere of space, assuming spherical geometry and a distance to the group of 80 Mpc.

In contrast to the H $\alpha$  luminosity, the B luminosity is more sensitive to the older stellar population of a system (Larson & Tinsley 1978). Using the formula proposed by Gallagher & Hunter (1984) it is possible to derive the star formation rate averaged for a period of  $10^9$  years:  $\text{SFR}(L_B) = 0.29 \times 10^{-10} L_B (M_\odot \text{yr}^{-1} L_\odot^{-1})$ . The ratio  $\text{SFR}(L_B) / \text{SFR}(L_{H_\alpha})$  gives a rough measure of the evolution of the star-formation rate inside the emission-line region during the last billion years. The star formation rates are listed in columns 7 and 8 of Table 2 and are discussed in section 4.3.

TABLE 3  
PHOTOMETRIC AND KINEMATIC PARAMETERS FOR THE TIDAL DWARF CANDIDATES

ID	PA $\pm$ ( $5^\circ$ )	Incl ( $^\circ$ )	$L_B$ ( $10^7 L_\odot$ )	$Rh_{75}$ (kpc)	$Dh_{75}$ (kpc)	$V_{max}$ ( $\text{km s}^{-1}$ )	Mass ( $10^8 M_\odot$ )	Mass/ $L_B$ ( $M_\odot/L_\odot$ )	$M_{tid}$ ( $10^8 M_\odot$ )
2-5	125	$55 \pm 10$	6.2	6.5	23	50	38	6	123
6	130	$60 \pm 15$	2.7	3.5	24	50	20	7	12
8	-5	$60 \pm 5$	1.9	4.5	13	115	138	73	225
20	70	$65 \pm 10$	0.4	3.2	23	30	6.7	17	15
21	80	$60 \pm 5$	1.4	3.5	27	55	24	17	12
22	75	$55 \pm 10$	0.9	3.0	24	25	4.3	5	11
23	40	$50 \pm 10$	0.4	2.0	23	23	2.4	6	3.6

#### 4.1. Masses, mass-to-light ratios and escape velocities

The fate of a tidal dwarf galaxy is basically driven by the ratio of its mass to the virial mass and the ratio of its mass to the so called tidal mass (Binney and Tremaine 1987, Duc 1995). The virial mass condition tells us if the tidal dwarf candidate is massive enough to be gravitationally stable against internal motions. The tidal mass condition will tell us if it is massive enough to survive the tidal forces exerted by the parent galaxy. In this work we only estimate the tidal mass since for the virial mass we would need a measurement of the internal velocity dispersion of the galaxy which we do not have.

In Table 3 we give, for each dwarf-galaxy candidate, in (1) the region identification number, (2) the position angle (3), the inclination (4) the total luminosity of the region, in the B band, measured inside an aperture of size similar to that within which the ionized gas was measured, (5) the radius  $R$  that corresponds to the maximum rotational velocity (except for region 22, where  $R$  is the radius within which emission was detected), (6) the distance to the parent galaxy, (7) the maximum rotational velocity (derived from the rotation curves, shown in Fig. 4), (8) the total galaxy mass, (9) the mass-to-light ratio and (10) the tidal mass.

The values given in columns (6), (8) and (10) are based on the following assumptions: 1) the tidal dwarf galaxy candidate was drawn from material from galaxy N7318B (or N7319 only for region 6), 2) the dwarf candidate presents a velocity gradient due to rotation, it is virialized, and therefore a value for the mass can be derived from the rotation curve, and 3) galaxies N7319 and N7318B have masses of  $1.3$  and  $1.8 \times 10^{11} M_\odot$  respectively (see below).

**Total masses of the tidal dwarf galaxy candidates:** We estimated the total mass of the candidate tidal dwarf galaxies from their rotation curves, derived from the velocity fields (Figs. 3a-3f) using the simple virial estimator (Lequeux 1983) in which the mass within a radius  $R$  of a rotating disk system is given by  $M(R) = f \times R \times V(R)^2 \times G^{-1}$ . Here  $V(R)$  is the rotational velocity at radius  $R$ ,  $G$  the gravitational constant and  $f$  is a constant value between 0.5 and 1. We chose a value of 1 for simplicity.

$M(R)$  is a lower limit on the estimate of the mass, since most likely these regions are not pure rotators. Random motions of the gas could provide significant dynamical support for the tidal dwarf galaxies as indicated by their line

widths. As an approximation, if we assume that the gas is in equilibrium, and that the gas velocity ellipsoid is isotropic, a very rough estimate of the contribution from the pressure support could be made using an ‘‘asymmetric drift correction’’ following Oort (1965). For gaseous objects in formation, such as those present in the Stephan’s quintet, and under the above assumptions, a general rule may be: 1) for rotation curves with amplitudes  $V_{max} \sim 25 \text{ km s}^{-1}$ , i.e. for the most internal regions of the self gravitating structures or for the least massive objects, the contributions from the dispersion and the rotation components may be comparable; 2) for  $V_{max} \sim 50 \text{ km s}^{-1}$ , the contribution of the dispersion velocity component may be approximately half of that for the rotational velocity component and 3) for  $V_{max} > 50 \text{ km s}^{-1}$ , i.e. at larger distances from the center of the objects and/or for more massive structures, the dispersion velocity may be negligible at first approximation.

**M/L of the tidal dwarf galaxy candidates:** The mass-to-light ratios of the candidate dwarf galaxies were obtained by dividing the values in column 8 by those in column 4 of Table 3. The median value for the mass-to-light ratios of the tidal dwarf galaxy candidates is  $7 M_\odot/L_\odot$ , with a large scatter, with values as high as  $74 M_\odot/L_\odot$  for region 8. The mass-to-light ratio of region 8 reflects its steep velocity gradient of  $\sim 26 \text{ h}_{75} \text{ km s}^{-1} \text{ kpc}^{-1}$ , the highest observed among the tidal dwarf candidates observed (see a discussion of this point in section 4.4).

**Total masses of the progenitor galaxies:** In order to determine the tidal masses, an estimate of the total mass of the progenitor galaxies is necessary. As we were not able to measure the rotation curves of the parent galaxies N7319 and N7318B due to the lack of ionized gas in their disks, we estimated their masses using the Tully-Fisher relation ( $M_B = -5.85 \log(2 V_{max}) - 5.61$ , Pierini (1999), the factor 2 within the log was included to match our definition of  $V_{max}$  to theirs). For absolute magnitudes of  $-21.4$  and  $-21.3$  and  $R_{25}$  of  $10.4$  and  $13.2 \text{ h}_{75} \text{ kpc}$  for N7319 and N7318B respectively we obtain maximum velocities of  $249$  and  $240 \text{ km s}^{-1}$ . Using the virial estimator we then obtain masses of  $1.3$  and  $1.8 \times 10^{11} M_\odot$ .

**Tidal masses:** The tidal masses listed in column 10 of Table 3 were derived from Binney and Tremaine (1987),  $M_{tid} = 3M(R/D)^3$ , where  $M$  is the mass of the parent

galaxy,  $R$  the radius of the tidal dwarf and  $D$  the distance to the parent galaxy. We assumed that the masses of the parent galaxies NGC 7318B (for regions 2-3-4-5, 8, 20, 21, 22 and 23) and NGC 7319 (for region 6) are  $1.3$  and  $1.8 \times 10^{11} M_{\odot}$  respectively, as calculated above. The results in Table 3 show that the dwarf masses determined are in two cases larger than the tidal masses (for regions 6 and 21), suggesting that the regions considered may survive tidal forces. This is not the case, however, for the complex of regions 2-5 and for regions 8, 20 and 22, for which the tidal mass is larger than the total mass estimated.

**Escape velocities of the candidates:** We can also estimate the escape velocity of the tidal dwarf candidates and compare this velocity to the systemic velocity difference between the dwarf candidate and the parent galaxy. We have found that the velocity difference between region 21 and N7318B is of the order of the escape velocity calculated at the distance of the region ( $27 \text{ h}^{-1} \text{ kpc}$ ), indicating that it may be able to escape from the parent galaxy potential. This is not the case for regions 2-5 and 6 (for the latter N7319 is the parent galaxy). For regions 8, 20, 22 and 23 we do not have an unique systemic velocity determination. Nevertheless we can give some estimate based on the possible systemic velocities (see Plana et al. 1999). For these four regions (8, 20, 22 and 23), the minimum possible velocities are  $\sim 5935, 5855, 5975$  and  $5935 \text{ km s}^{-1}$ , respectively (Plana et al. 1999, their Table 1). If we assume that NGC 7318B (with velocity  $5774 \text{ km s}^{-1}$ ) is the parent galaxy, then the differences between the velocity of the parent galaxy and that for each of the tidal dwarf candidates are  $161, 81, 201$  and  $161 \text{ km s}^{-1}$  (or larger) for regions 8, 20, 22 and 23 respectively. On the other hand, the escape velocities are  $344, 259, 253$  and  $259 \text{ km s}^{-1}$  respectively. Therefore, if the minimum possible velocities are the true radial velocities, only region 22 of the four may be able to escape the potential of the parent galaxy, since for this region the escape velocity is similar to the velocity difference. We then conclude that only two out of the seven candidates may have velocities such that they can escape the gravitational field of the parent galaxy.

#### 4.2. Comparison of the velocity fields

Just a few kinematic studies are available on tidal dwarf galaxies and dwarf galaxies in general. Duc and Mirabel (1998) showed velocity curves of dwarf galaxies around NGC 5291 measured from HI kinematics. The curves show in general stronger gradients than those measured for the galaxies in Stephan's quintet. However, the diameter of the objects, as computed from the optical images, are similar.

Another set of velocity curves and rotation curves for dwarf galaxies comes from Östlin et al. (1999) and Östlin et al. (2000). Their sample is composed of luminous blue compact galaxies (hereafter BCG's). The radial extent of the rotation curves are comparable to those for the candidate tidal dwarf galaxies in Stephan's quintet and the velocity amplitudes also seem to be similar. The shapes of the rotation curves, however, are very different. While in our sample the rotation curves show in general a typical shape for solid body rotation, in Östlin et al. (1999) the rotation curves of the BCG's have flat plateaus.

In Östlin et al. (1999, 2000), the velocity fields are irreg-

ular and often contain secondary dynamical components although they in most cases display overall rotation. By comparison of the stellar masses (by means of multicolor images and spectral evolutionary synthesis' analysis) to the total masses of the galaxies (derived from the rotation curves), they showed that at least half of the galaxies cannot be supported by rotation. They found that the morphologies and dynamics of the BCG's suggest that the starburst activity in these galaxies are most likely triggered by mergers of dwarf galaxies and/or massive gas clouds. In the case of the candidate tidal dwarf galaxies, it is possible that they are also partially supported by random motions as it is the case for the BCG's. Moreover, the starburst activity in the tidal dwarf galaxies could also be nurtured by merging of gas clouds during the ongoing tidal process.

Hunter et al. (2000) have recently made a compilation of possible dwarf galaxies in many different environments which could have tidal origin. A comparison of the maximum rotation velocities as a function of the B absolute magnitudes of the tidal dwarf galaxy candidates in Stephan's quintet and galaxies in Hunter's sample is shown in Fig. 5. As can be seen, the velocities and magnitudes of the H92's tidal dwarf candidates are within the ranges of parameters of other possible candidates.

#### 4.3. Comparison of the SFR for various classes of emission-line objects

There are several classes of emission-line objects which have similarities in some respects with the objects we observed in Stephan's quintet.

A comparison of the star formation rates (SFR) for five samples of dwarf galaxies, one sample of HII regions in nearby spiral galaxies and our sample is shown in Fig. 6. We identified each of the galaxies in our sample with its corresponding ID number. Included in the comparison are (1) a sample of irregular galaxies from the Local Group (Mateo 1998), (2) a sample of isolated irregular galaxies of low luminosity and central surface densities, (3) a sample of blue compact galaxies studied by Sage et al. (1992) with blue luminosities similar to the systems observed in Stephan's quintet, (4) another sample of blue compact galaxies studied by Östlin et al. (1999), (5) a sample of tidal dwarf galaxy candidates around N5291 studied by Duc and Mirabel (1998), and (6) a sample of HII regions in the spiral galaxies NGC 1365, NGC 1566, NGC 2366, NGC 2903, NGC 2997, NGC 3351, NGC 4303, NGC 4449, NGC 5253 studied by Mayya (1994, their table 1, only objects with data quality 1 or 2 were included).

Fig. 6 shows that the Local Group and isolated irregular galaxies have  $\text{SFR}(H\alpha)$ 's that are on average lower than those for all the other samples. HII regions in nearby galaxies and blue compact galaxies have values for the  $\text{SFR}(H\alpha)$  in between those observed for isolated galaxies and those for tidal dwarf galaxies and giant HII regions of Stephan's quintet. While in the sample of Sage et al. (1992) the blue compact galaxies have a comparable range of luminosities to the galaxies in the other samples, Östlin et al.'s sample is dominated by blue compact galaxies with high B-luminosities. Still, the  $\text{SFR}(H\alpha)$  for these two samples agree in the region of overlap. The faintest blue compact galaxies seem to overlap with the location of the figure occupied by the HII regions in nearby spi-



ral galaxies, although the latter extend to much lower luminosities. The tidal dwarf galaxies studied by Duc & Mirabel (1998) have average  $\text{SFR}(H\alpha)$ 's that are comparable to the objects studied in this paper. However, Duc & Mirabel's measurements were made through long slit observations and the values may be a lower limit on the  $H\alpha$  fluxes and therefore to the  $\text{SFR}(H\alpha)$ 's derived for these galaxies.

The  $\text{SFR}(H\alpha)$ 's for the BCG's may be affected by dust, which would artificially lower the rates derived for these objects. Therefore, in reality, the  $\text{SFR}(H\alpha)$ 's for tidal dwarf galaxies and BCG's may be similar although these galaxies are fundamentally two distinct classes (for instance they have completely different metallicities, with the BCG's being metal poor objects and the tidal dwarf galaxies having the high metallicities of their parent galaxies). One should also be aware that there exists a very large range of  $\text{SFR}(H\alpha)$ 's for both the BCG's and the tidal dwarf galaxies. Only a crude comparison between the  $\text{SFR}(H\alpha)$ 's of the two populations is then possible.

#### 4.4. Considerations about streaming motions in tidal tails

Region 8 as well as the complex of regions 2–5 seem to be a part of a tidal tail. In addition, region 6 may be at the edge of a tidal tail, if we assume that it is associated with N7318A and not with N7319 (see section 4.7). One obvious concern is then that the observed velocity gradients for these regions could be a result of streaming motion in the tail within which the region is embedded.

In the case of region 8, if we assume that it is attached to N7318B (at a velocity of  $\sim 5700 \text{ km s}^{-1}$ ) and it has a velocity of  $\sim 5900 \text{ km s}^{-1}$  (J. Sulentic, private communication), the gradient of the motion in the tidal tail (lower velocities in the south and higher velocities in the north) has opposite sense to what is observed in the region itself (the red side of the region is to the south, see Fig. 3c). This represents clear evidence that the strong velocity gradient observed for region 8 cannot be due to streaming motions within the tidal tail. In addition, we note that there is a large misalignment of at least 30 degrees between the PA of the major axis of region 8 and that of the tidal tail within which it seems to be embedded (see Fig. 1a). This again indicates that region 8 cannot be just a part of a tidal tail and it is, instead, an object with its own rotation pattern.

In the case of the complex of regions 2–5, we find that the velocity gradient we observed for it (these regions are located at the edge of a tidal tail that emanates from the northern arm of N7318B) could not be strongly affected by streaming motions for the following reason. For this complex we have information on the HI velocity field kindly provided by L. Verdes-Montenegro (private communication). The motion observed in HI encompasses an area that goes from the base of the northern tail of N7318B to our region 1 and it has a very similar mean radial velocity ( $\sim 6000 \text{ km s}^{-1}$ ) to that of the  $H\alpha$  emission in complex 2–5. We compared the  $H\alpha$  and the HI velocity fields for regions 2–5 and we found that while the  $H\alpha$  gradient reaches  $50 \text{ km s}^{-1}$  over a radius of 13 arcsec in extent, the HI gradient reaches only about  $15 \text{ km s}^{-1}$  over the same area. Assuming that the HI velocity gradient gives us an upper limit on the large-scale motion of the tidal tail (up-

per limit because some internal motion is also expected to be present in the HI component) the difference between the two gradients ( $35 \text{ km s}^{-1}$ ) is due to internal motions within the complex 2–5. With this correction the new mass-to-light ratio of the complex of regions 2–5 would be  $3 M_{\odot}/L_{\odot}$ .

In a scenario where region 6 were at the edge of the tidal tail that emanates from N7318A, there would be no concern about its velocity gradient being due to streaming motion since the center of the parent galaxy and region 6 have almost exactly the same velocity.

We conclude that streaming motions within the tails may not significantly change the observed velocity gradients measured in this study.

#### 4.5. Other dynamic considerations

Dubinski et al. (1999) find that a good criterion for making tidal tails during a collision appears to be that the ratio of the escape velocity ( $V_e$ ) over the circular velocity ( $V_{max}$ , in our notation) of the galaxy, measured at a radius of  $2R_d$ , must be lower than 2.5 ( $R_d$  is the scale length of the galaxy). According to Dubinski et al. (1999) this condition is valid for a wide range of models including those with disk-dominated and halo-dominated rotation curves. They also find that galaxies with declining rotation curves are the best candidates to produce tidal tails during collisions. We do not have information on the rotation curves of the galaxies (due to their lack of ionized gas) but we can still check the velocity ratio condition  $V_{esc}/V_{max} < 2.5$  assuming that the galaxies follow the Tully-Fisher relation (see Section 4.1). The masses inside  $2R_d$  are 1.1 and  $0.8 \times 10^{11}$  for N7318B and N7319 respectively (if we assume that the scale length of the galaxies  $R_d \sim R_{25}/3.2$ ). The ratio  $V_{esc}/V_{max}$  is, then, well below 2.5 for both galaxies, indicating that they may develop tidal tails during collisions. This is a comfortable confirmation since both galaxies obviously have developed one or more tidal tails.

It is interesting to note that the inclination of the seven tidal dwarf candidates lie in between the values of  $50^\circ$  and  $65^\circ$ , which are very similar to the inclinations of the progenitor galaxies of  $59^\circ$  and  $66^\circ$  (from the Lyon-Meudon Extragalactic Database, LEDA), for N7319 and N7318B respectively. If the candidate tidal dwarf galaxies are formed in the plane of the disks of the parent galaxies, they probably could keep the angular momentum of their progenitor disks. This inclination concordance would then be expected by the conservation of angular momentum of the system. However, the inclination found for the candidates could be biased by the fact that standard methods for deriving inclinations favor high values of inclination (low inclination values are harder to be determined). In addition, since we do not have information on which side of the galaxy is pointing to us, the two inclined disks with  $60^\circ$  inclinations could actually be separated by  $120^\circ$ !

#### 4.6. Summary of the properties of the tidal dwarf galaxy candidates

Table 4 summarizes the characteristics of each of the seven tidal dwarf candidates of Stephan's quintet. A "plus" in an entry means (1) In column two if the color is bluer than  $B-R = 0.8$ , (2) in column 3 if the  $\text{SFR}(H\alpha)/\text{SFR}(L_B)$  (see section 3.4) is typical of a tidal

TABLE 4  
SUMMARY OF THE PROPERTIES OF THE TIDAL DWARF GALAXIES

ID	Blue Color	SFR(H $\alpha$ )/SFR(L $B$ ) condition	Velocity Gradient condition	$M_{tidal}$	$V_{esc}$ condition	Location	associated w/ HI cloud?
2-5	+	+	+	-	-	End of tail	+
6	-	+	+	+	-	End of tail	+
8	+	+	+	-	-	Inside a tail	-
20	+	+	+	-	-	Isolated	-
21	+	+	+	+	+	Isolated	-
22	+	+	+	-	+	Isolated	-
23	+	+	+	-	-	Isolated	-

dwarf galaxy, (3) in column 4, if the galaxy presents a velocity gradient larger than  $8.0 \text{ h}_{75} \text{ km s}^{-1} \text{ kpc}^{-1}$  (this will be true for all of the objects since they were classified as tidal dwarf candidates based on the presence of the velocity gradients), (4) in column 5 if the mass of the galaxy as measured from the internal kinematics of the ionized gas is larger than the tidal mass obtained in section 4.1, (5) in column 6 if the escape velocity of the parent galaxy is lower than the velocity difference between the systemic velocity of the tidal dwarf candidate and that of the parent galaxy (assuming that the parent galaxy is N7318B for all regions except for region 6, for which the parent galaxy is assumed to be N7319). The last two columns of Table 4 mark if the candidate belongs to a tidal tail and if it is associated with an HI cloud.

Regions 6 and 21 seem to be the ones with the highest chance of surviving as single entities. This is specially true for region 6 where CO emission at the redshift and location of the galaxy has been recently detected (Gao & Xu 2000) indicating a molecular gas mass of a few times  $10^8 M_{\odot}$ . Other less massive candidates like regions 20, 22 and 23 may not be massive enough to become independent entities. However, we should keep in mind that the values for the mass were determined under the assumption the regions are pure planar rotators and hence these are lower limits. In fact, random motions of the gas and stars may provide significant dynamical support for the tidal dwarf galaxies as indicated by their line widths. Larger values for the mass of the candidates (obtained if the internal dispersion velocity is also taken into account) would result in an increase of the number of objects that could survive.

Although the complex of regions 2-5 may not survive as a single entity (the tidal mass is very large mainly because of the large radius of the complex), it may be split into several smaller candidates which could then survive the tidal forces exerted by N7318B.

#### 4.7. Other probable tidal dwarf galaxy candidates

The HI map of Stephan's quintet presented by Williams et al. (1999, their Fig. 5) shows that the HI component at velocity  $6600\text{--}6700 \text{ km s}^{-1}$  is distributed along a fragmented ring around the galaxy N7319, possibly formed after a tidal interaction with N7320C. Such HI rings have previously been observed in other interacting systems like e.g. N5291 (Malphrus et al. 1997). The northwestern side

of the HI ring overlaps with the dwarf galaxy candidate identified as Region 6. It is possible that there are other tidal dwarf galaxy candidates along what would be the continuation of the ring, to the north, beyond region 6, north of N7319, where HI is not measured by Williams et al. (1999).

Comparing the eastern side of the HI ring with an optical image of the quintet we notice that the end of the tidal tail of N7319 that points to N7320C (in the southeastern side of the group) has a number of optical condensations (Hunsberger et al. 1996, Gallagher et al. 2000) that overlaps with maxima in the HI distribution. These regions probably have similar velocities to that of the HI gas ( $6700 \text{ km s}^{-1}$ ) and are most likely tidal dwarf candidates formed during a past encounter between N7319 and N7320C. Other faint condensations can be seen in this region, between N7319 and N7320C. The velocities of these objects have to be measured in order to confirm their nature.

What is very intriguing at first is the exact superposition of the HI component at  $6700 \text{ km s}^{-1}$  with the galaxy NGC 7320, at  $800 \text{ km s}^{-1}$ . This superposition may be understood if the following is considered. Moles et al. (1998) noted that while in a narrow-band image (e.g. H $\alpha$ ) the galaxy NGC 7320 appeared symmetric, in a broad-band image it appeared very asymmetric, showing an extension to its northwest. In fact, what may appear to be the northwestern extension of the nearby galaxy N7320 in broad-band images may be in reality a chain of smaller background objects (perhaps other tidal dwarf galaxy candidates?) superimposed on the line of sight, but with velocities that coincide with that of the HI component at  $6700 \text{ km s}^{-1}$ . Other regions may have velocities of  $\sim 5700 \text{ km s}^{-1}$  (possibly associated with N7318B). Support for this scenario comes from the mix of velocities measured in this region by Moles et al. (1998). Again, more velocity measurements of the condensations present in this region are needed.

Other tidal dwarf galaxies may be associated with N7318A. Although Moles et al. (1998) did not consider this galaxy in the interacting history of the quintet, it must have been part of collisions given the peculiar pattern of dust seen in the HST image (Charlton et al. 2000) and due to the several linear features that seem to emanate from the galaxy. These were marked with arrows in Fig. 1c. A

few of these could be projected material from N7318A into the intragroup medium, in the same way it has been observed for Arp 105 by Duc (1995). Alternatively it could be material in the process of re-accretion onto the parent galaxy after an interaction. There seems to be two different types of linear features, a few that are long and filamentary, with very low surface brightnesses and others that are small and have high surface brightnesses. Perhaps also region 6 may be born out of gas from N7318A and not of N7319 as it has been assumed throughout this paper. This would be a specially appealing scenario if we could confirm that there is material in between galaxy N7318A and region 6 at a common velocity (of  $\sim 6700 \text{ km s}^{-1}$ ). However, it is more probable (see Fig. 2 of Xu et al. 1999) that the apparent optical connection between regions 8 and 4 (seen as a filament in the HST image) is at a lower velocity of  $5900\text{--}6000 \text{ km s}^{-1}$ . Also important would be to confirm if the features marked in Fig. 1c coincide with the velocity of N7318A.

We would also like to point out that the emission detected in regions 7 and 9 and in the features in between these two regions might be associated with the higher velocity component of the group at  $6700 \text{ km s}^{-1}$  instead of being related to the lower velocity component (as it has been assumed in this paper). This is supported by the  $\text{H}\alpha\text{--}[\text{NII}]$  map presented by Xu et al. (1999, their Fig. 2), which shows clearly that these regions are dominated by emission from the high-velocity component. Further indirect evidence is their low  $\text{H}\alpha$  content despite their high optical luminosities (see Fig. 1a and 1c), which suggests that the emission from this area may perhaps fall at the very edge of the CFHT filter, where the transmission is minimum. These regions would not have been detected in the lower S/N data taken with the SAO 6m, where only very bright sources like region 6 were detected. As can be seen from Fig. 1c the *optical* luminosities of the sources in the area in between regions 7 and 9 are comparable to those of other regions identified by us. This only illustrates the incredible mixture of matter at two different velocities in this group.

#### 4.8. *Properties of region 6 in a scenario where N7318A is the parent galaxy*

We assumed in the previous sections that region 6 is formed of remnant gas from N7319 (Moles et al. 1997). We favored this scenario based on the evidence from the HI observations (Fig. 5 from Williams et al. 1999) which showed a structure similar to a ring (an HI incomplete ring) around galaxy N7319. The HI gas associated with region 6 seems to be part of this large ring, in which case region 6 would be formed from gas originally in N7319. On the other hand, there is also the possibility that region 6 was formed from gas spelled from N7318A. Support for this is given by Fig. 1c, where linear features apparently associated with N7318A are seen. In this scenario region 6 might be located at the tip of a tidal tail that may originate at the northern arm of N7318A. We need new velocity measurements of the region to decide between the two scenarios.

In the following we give the parameters for region 6 in the case where it is physically associated with N7318A: (1) it would be at a distance of  $25 \text{ h}_{75}^{-1} \text{ kpc}$  to the par-

ent galaxy; (2) it would have a tidal mass of  $6 \times 10^8 M_{\odot}$ , smaller than its inferred mass; (3) the difference between its radial velocity and that of the parent galaxy is still lower than the escape velocity of the parent galaxy; (4) its inclination ( $60^{\circ} \pm 15^{\circ}$ ) would still be similar to (within the errors) to that measured for the parent galaxy ( $49^{\circ}$ , value taken from the Lyon-Meudon Extragalactic Database, LEDA).

## 5. SUMMARY

We presented B and R photometry and a Fabry-Perot  $\text{H}\alpha$  map of 23 emission-line regions in Stephan's quintet. All but one region may be associated with N7318B (region 6 may be attached either to N7319 or to N7318A).

Our main results are:

- We find that seven of the regions have velocity gradients greater than  $8 \text{ h}_{75} \text{ km s}^{-1} \text{ kpc}^{-1}$ . We classify those as tidal dwarf galaxy candidates.
- Two tidal dwarf candidates may be located at the edge of a tidal tail, one within a tail and for four others there is no obvious stellar/gaseous bridge between them and the parent galaxy.
- Two of the candidates are associated with HI clouds, one of which is, in addition, associated with a CO cloud.
- The tidal dwarf candidates have low continuum fluxes and high  $\text{H}\alpha$  luminosity densities of  $F(\text{H}\alpha) = 1 - 60 \times 10^{-14} \text{ erg s}^{-1} \text{ cm}^{-2}$ , magnitudes of  $M_B = -16.1$  to  $-12.6$ , sizes of typically  $\sim 3.5 \text{ h}_{75}^{-1} \text{ kpc}$ , colors  $B - R$  between 0.3 and 1.3, gas velocity gradients of  $\sim 8 - 26 \text{ h}_{75} \text{ km s}^{-1} \text{ kpc}^{-1}$ ,  $\text{SFR}(\text{H}\alpha)/\text{SFR}(L_B)$  between  $\sim 1100$  and  $6000$ , masses of  $\sim 2 \times 10^8$  to  $10^{10} M_{\odot}$  and a median mass-to-light ratio of  $7 M_{\odot}/L_{\odot}$ .
- The lower limits of the masses of the candidate tidal dwarf galaxies determined from their rotation curves (assuming that they are pure rotators) are in two cases larger than their tidal masses.
- Two out of the seven candidates may have velocities such that they can escape the gravitational field of the parent galaxy.
- Possible streaming motions within the tails may not have significantly affected the observed velocity gradients of those tidal dwarf candidates that are located within tails.
- The dynamical criterion for formation of tidal tails during a collision  $V_{esc}/V_{max} < 2.5$  is followed by galaxies NGC 7319 and NGC 7318B.

A few of the tidal dwarf galaxies we identified in this study may survive as single entities, leading to the formation of new group members of the Stephan's quintet.

We would like to thank Dr. Jacques Boulesteix and the SAO observatory staff (Drs V. Afanasiev, A. Burenkov, S. Dodonov, V. Vlasiuk and S. Drabek) for their help during the observations. We would also like to thank Drs.

S. Hunsberger, M. Marcelin and J. Sulentic for insightful discussions and Lourdes Verdes-Montenegro for sending us the HI map of the quintet. CMdO thanks the Marseille Observatory for their hospitality and funding of a trip in July 1999. PA thanks the Brazilian funding agency FAPESP for the financial support for two visits

to the Instituto Astronomico e Geofisico, project numbers 99/05514-3 and 99/03744-1. HP acknowledges the financial support of FAPESP through a pos-doc position, project number 96/06722-0, and the Mexican CONACYT under project 32303-E.

## REFERENCES

- Allen R.J., Sullivan III W.T., 1980, *A&A* 184, 181  
 Amram P., Boulesteix J., Marcelin M., Balkowski C., Cayatte, V., Sullivan W. T. III, 1995, *A&A Suppl.* 113, 35  
 Amram P., Balkowski C., Boulesteix J., Cayatte V., Marcelin M., Sullivan, W.T. III, 1996, *A&A* 310, 737  
 Amram P., Mendes de Oliveira C., Boulesteix J., Balkowski C., 1998, *A&A*, 330, 881  
 Aoki, K., Kosugi, G., Wilson, A. & Yoshida, M., 1999, *ApJ* 521, 565  
 Arp H., 1973, *ApJ* 183, 411  
 Balkowski C., Bottinelli L., Gouguenheim L., Heidmann J., 1973, *A&A* 25, 319  
 Bertin E. & Arnouts S. 1996, *A&A Suppl. Series*, 117, 393B  
 Binney, J. & Tremaine, S. 1987, *Galactic Dynamics* (Princeton: Princeton University Press)  
 Charlton, J., Knierman K., Hunsberger S., Gallagher S., Whitmore, B. Kundu, A., Hibbard, J. 2000, in *Celebrating 10 Years of HST*, symposium held in May 2000, in press.  
 Dubinski, J., Mihos, J.C., Hernquist, L., 1999, *ApJ* 526, 607  
 Duc P.A., 1995 PhD Thesis  
 Duc P.A., Mirabel, F., 1998, *A&A* 333, 813  
 Gallagher J.S., Hunter D.A., Tutukov A.V., 1984, *ApJ* 284, 544  
 Gallagher S.C., Hunsberger S.D., Charlton J.C., Zaritsky D., 2000 in "Massive Stellar Clusters" ASP Conf. Series in press (astro-ph/0002066)  
 Gao, Y. & Xu, C., 2000, *ApJ* 542, L83  
 Hibbard J.E. & van Gorkom J., 1996, *AJ* 111,655  
 Hickson P., Mendes de Oliveira C., Huchra J.P., Palumbo G.G.C., 1992, *ApJ* 399, 353  
 Hunsberger S.D., Charlton J.C., Zaritsky D., 1996, *ApJ*, 462, 50  
 Hunter D.A., Gallagher III J.S., 1986 *PASP* 98, 599  
 Hunter D.A., Hunsberger S.D., Roye E.W., 2000 astro-ph/0005257  
 Kron R. G., 1980, *ApJ Suppl. Series*, 43, 305  
 Landolt A.U. 1992, *AJ* 104, 340  
 Larson R. B. & Tinsley B. M., 1978, *ApJ* 219, 46  
 Lequeux J., 1983, *A&A* 125, 394  
 Malphrus, B., Simpson, C., Gottesman, S., & Hawarden, T.G., 1997, *AJ*, 114, 1427  
 Mateo, M. L., 1998, *ARA&A*, 36, 435  
 Mayya, Y.D., 1994, *AJ* 108, 1276  
 Moles M., Sulentic J.W., Márquez I. 1997, *ApJ*, 485, L69  
 Moles M., Márquez I., Sulentic J.W. 1998, *A&A*, 334, 473  
 Oort, 1965. In: *Star and Stellar Systems V: Galactic Structure*, edited by Blaauw and Schmitd, University of Chicago Press, p. 455.  
 Östlin G., Amram P., Masegosa J., Bergvall N., Boulesteix J., 1999, *A&A Suppl. Series* 137, 419  
 Östlin G., Amram P., Masegosa J., Bergvall N., Boulesteix J., Márquez, I. 2000, *A&A*, submitted  
 Pierini, D. 1999, *A&A* 352, 49  
 Plana H., Boulesteix J., Amram P., Carignan C., Mendes de Oliveira C. 1998, *A&AS*, 128, 75  
 Plana H., Mendes de Oliveira, C., Amram, P., Bolte, M., Balkowski, C. 1999, *ApJ* 516, L69  
 Sage I.J., Salzer J.J., Loose H.H., Henkel C., 1992 *A&A* 265, 19  
 Shostak G.S., Sullivan III, W.T. & Allen, R.J. 1984, *A&A* 139, 15  
 Williams, B.A., Van Gorkom, J.H., Yun, M., & Verdes-Montenegro, L. 1999, in *Galaxy Interactions at Low and High Redshift*, proceedings of the IAU Symposium 186, held at Kyoto, Japan, 26-30 August, 1997. Edited by J. E. Barnes, and D. B. Sanders, p.375  
 Xu C., Sulentic J. W., Tuffs R., 1999 *ApJ* 512, 178  
 Zwicky F., 1956, *Ergebnisse der Exakten Naturwissenschaften*, 29, 344

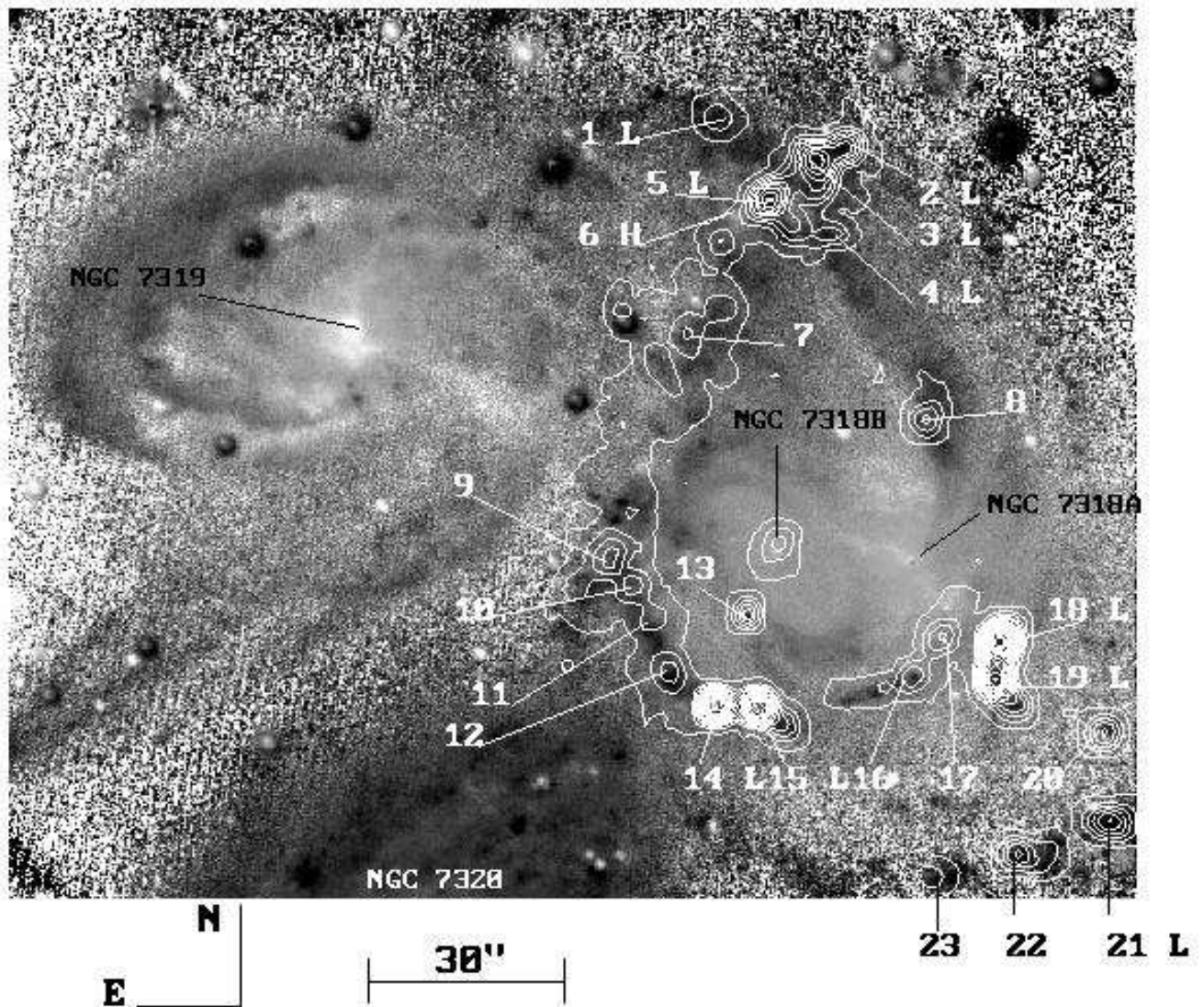


FIG. 1A.— (a) This figure presents the B–R color image. Dark is blue and white is red. The dimension of the image is  $3 \times 2.4$  arcmin. North is up and east is to the left. The  $H\alpha$  monochromatic emission contours are shown and the 23 emitting regions detected by Plana et al. 1999 are marked. An “L” (for low) marks regions known to have velocities in the range  $5700\text{--}6000 \text{ km s}^{-1}$  while an “H” (for high) marks region 6, the only region for which the velocity is confirmed to be  $\sim 6700 \text{ km s}^{-1}$ . The monochromatic contours are flux calibrated. The lowest level is  $4.2 \times 10^{-17} \text{ erg s}^{-1} \text{ cm}^{-2} \text{ arcsec}^{-2}$  and the step is  $1.7 \times 10^{-17} \text{ erg s}^{-1} \text{ cm}^{-2} \text{ arcsec}^{-2}$ . (b) This figure presents the R image of the group after sky subtraction. Optical blobs corresponding to  $H\alpha$  emitting regions are marked. (c) The final combined B image of the quintet. Linear features which could possibly be associated with N7318A are marked with arrows (see text).

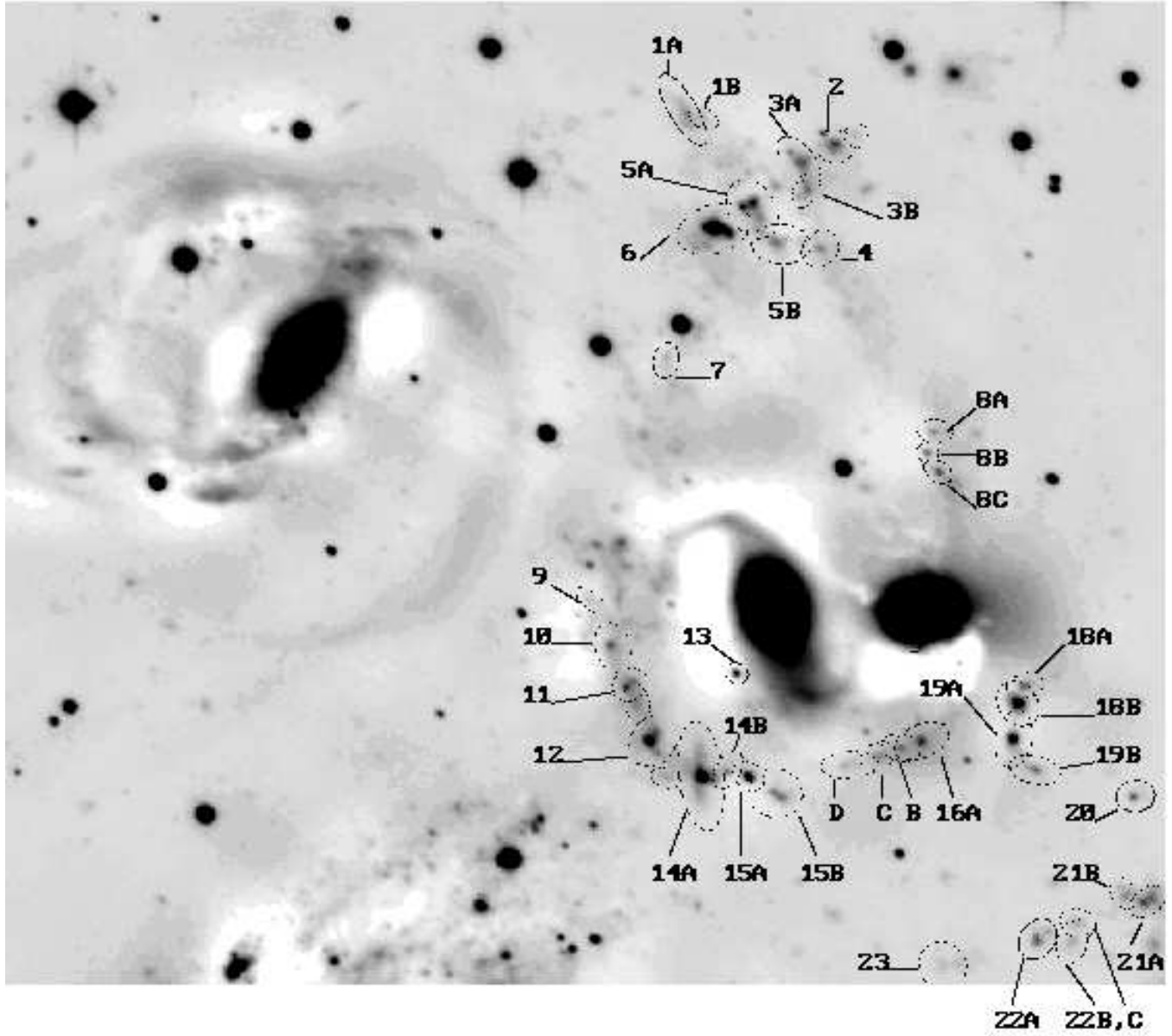


FIG. 1B.—

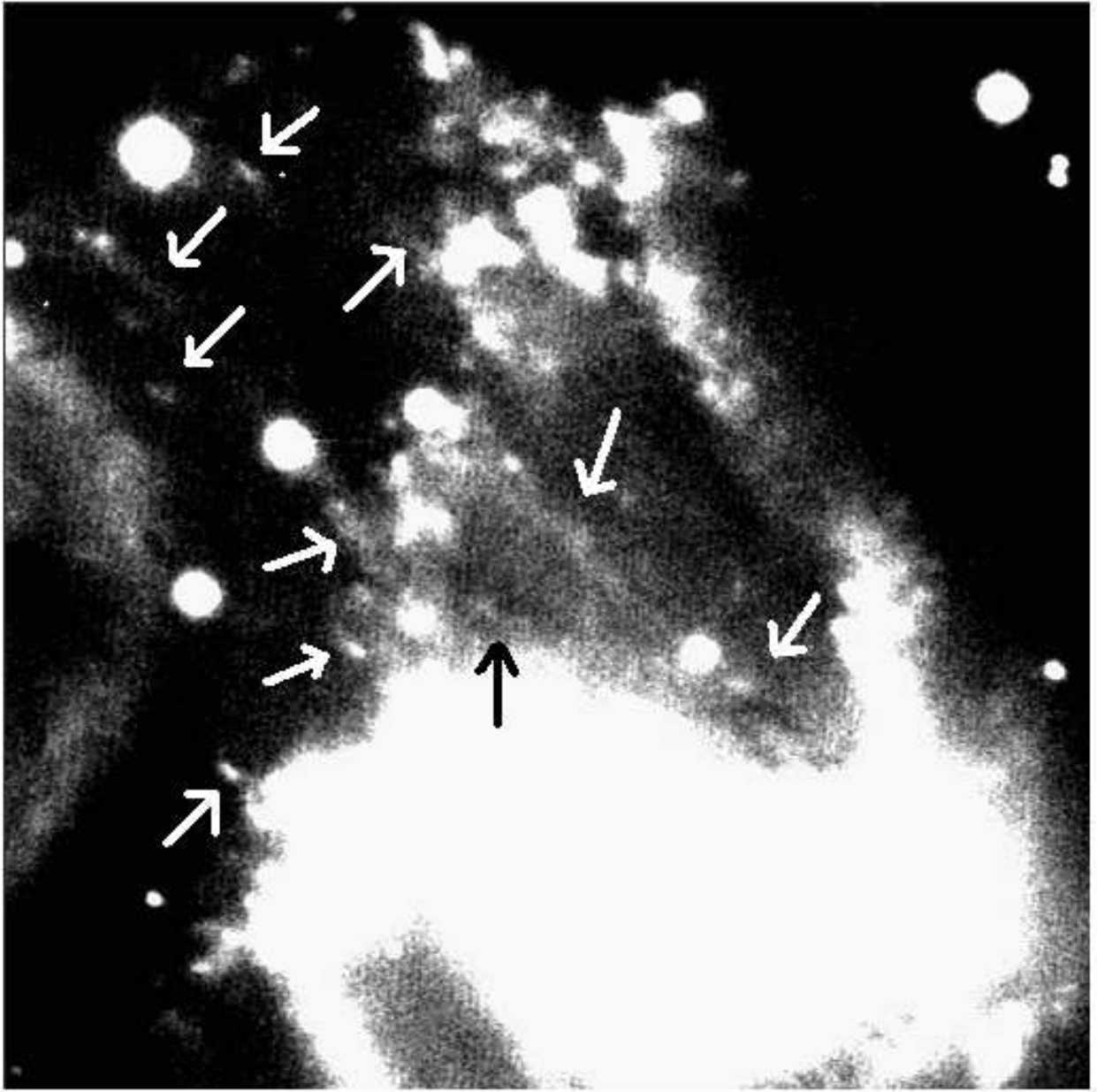


FIG. 1C.—

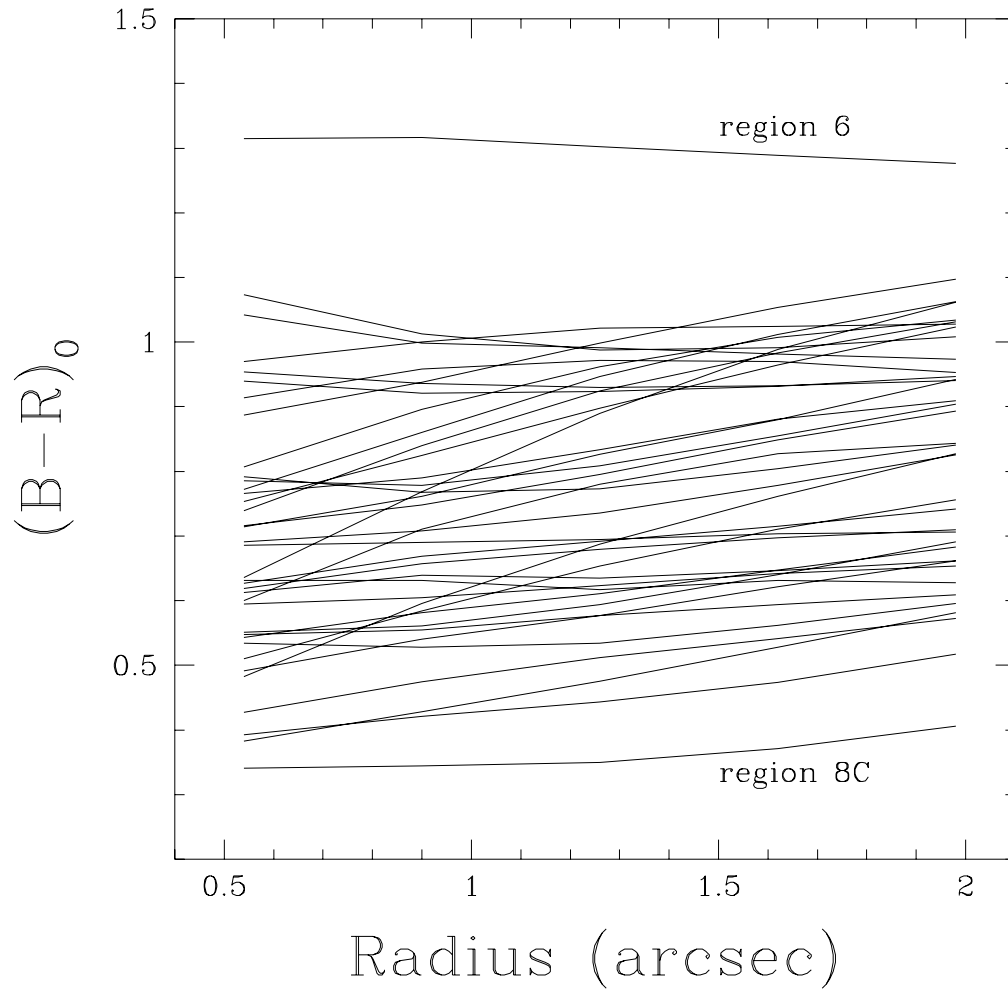


FIG. 2.— The corrected B–R color gradient for each emission-line blob identified in Fig. 1b (see text).



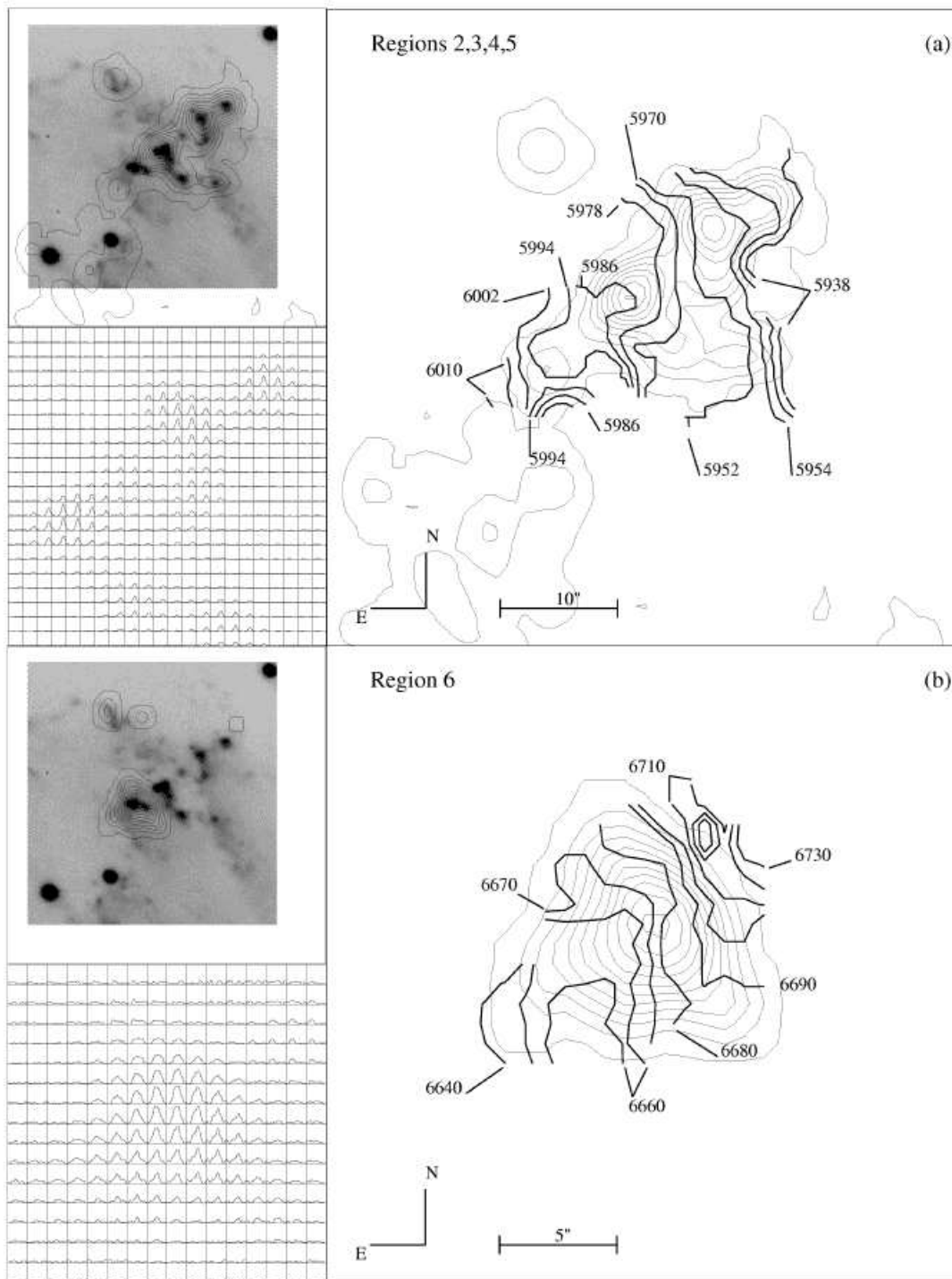


FIG. 3AB.— From (a) to (g) each figure presents the following. Upper left: B band image superimposed onto the monochromatic map; the isocontours are the same as those presented in Fig. 1a; lower left: profiles from the Fabry-Perot data cube – the pixel size is 0.86; right panel: the velocity field superimposed onto the monochromatic image. The field size for the right panel is the same as that for the upper left panel.

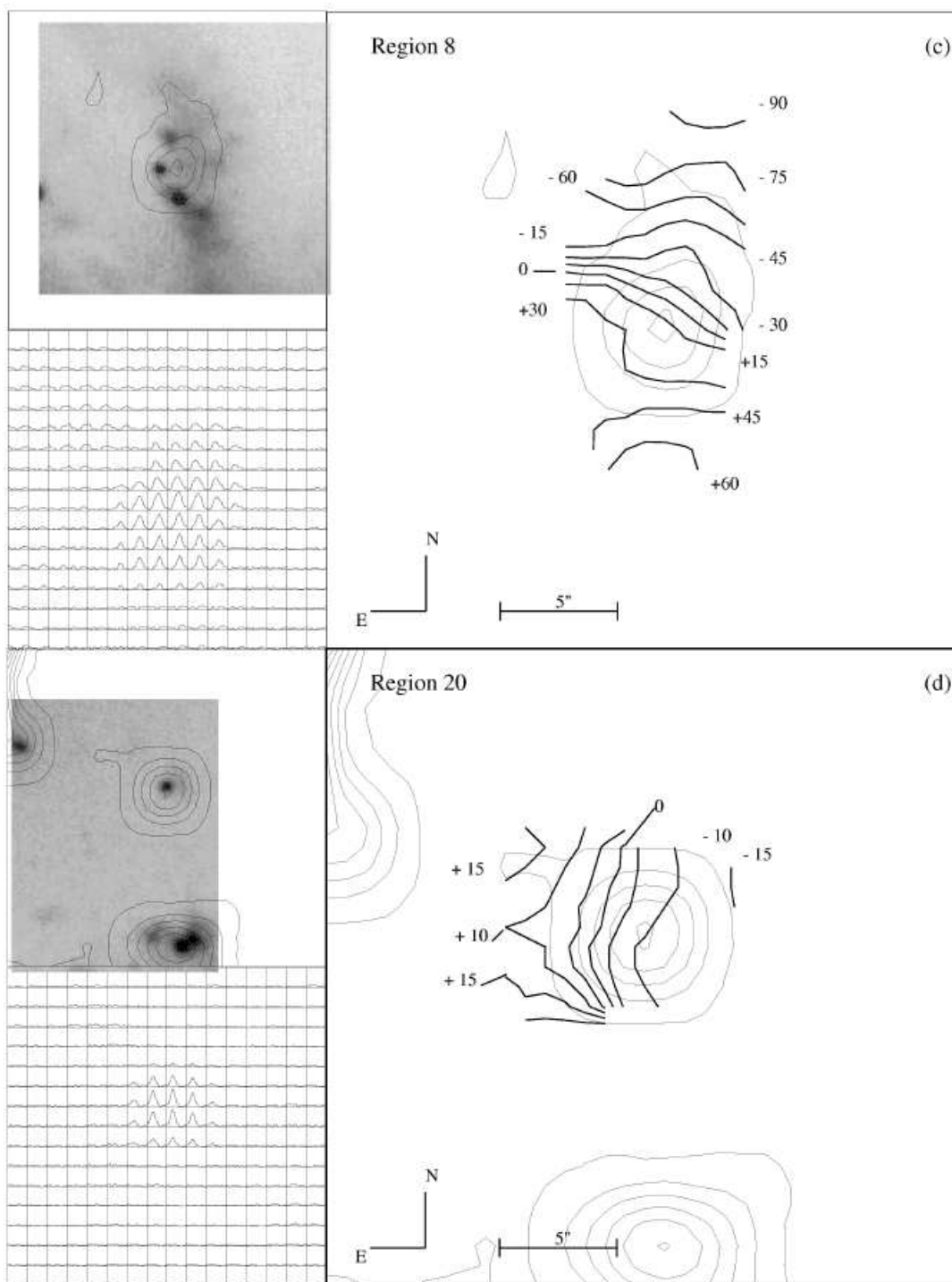


FIG. 3CD.—

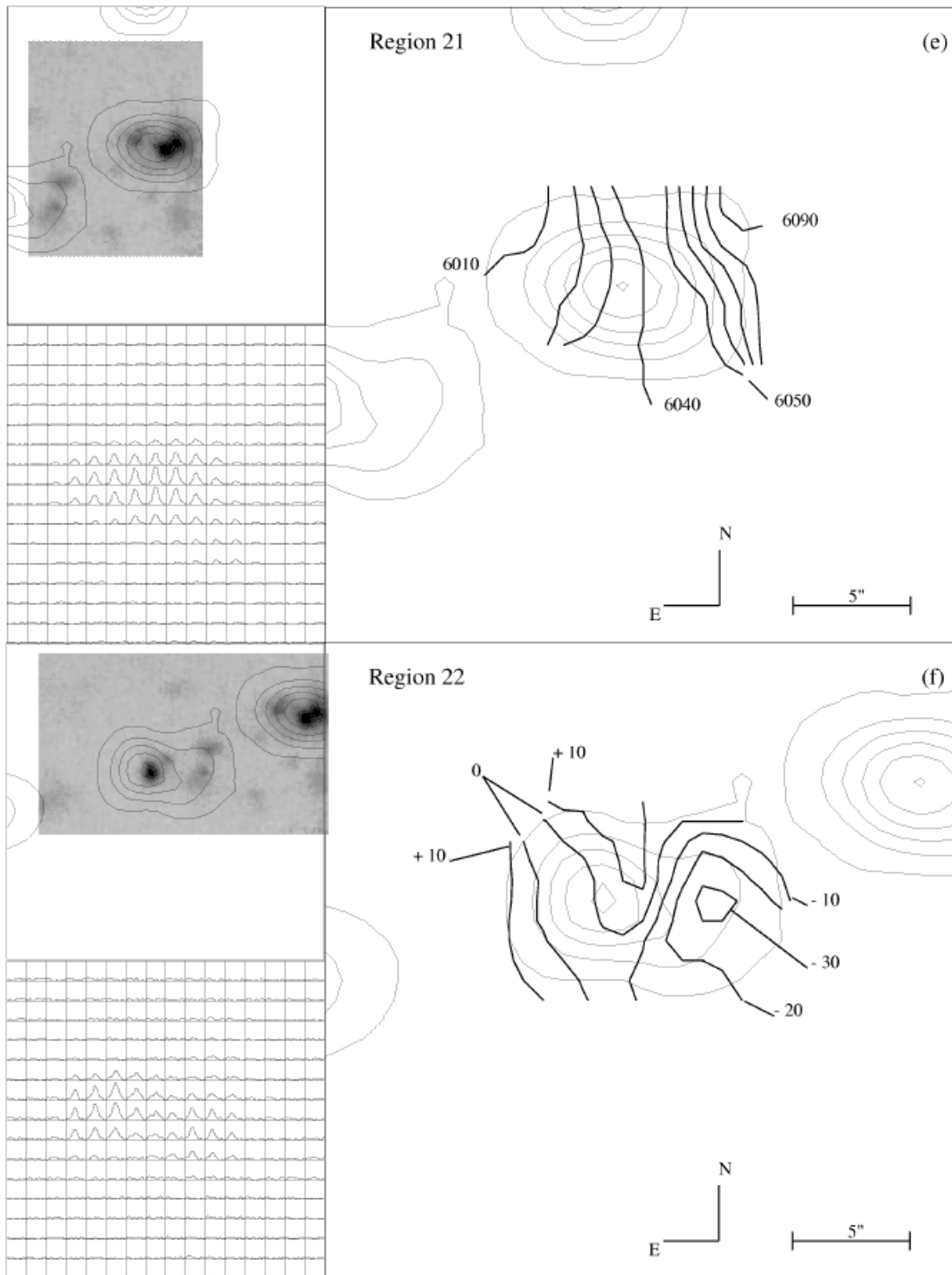


FIG. 3EF.—

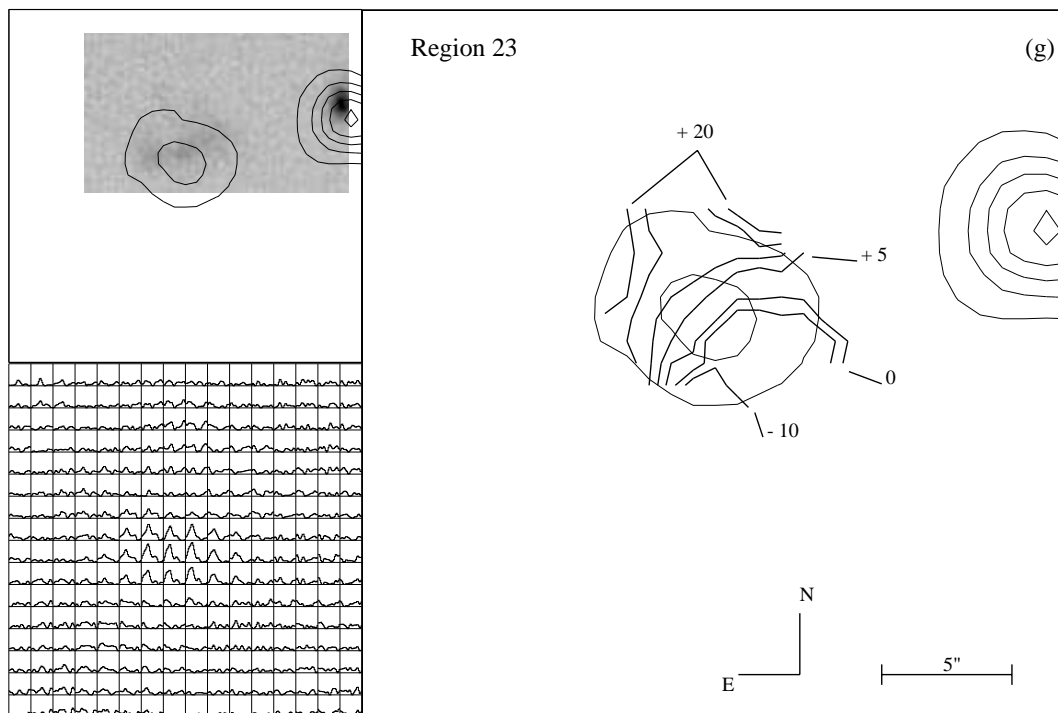


FIG. 3G.—

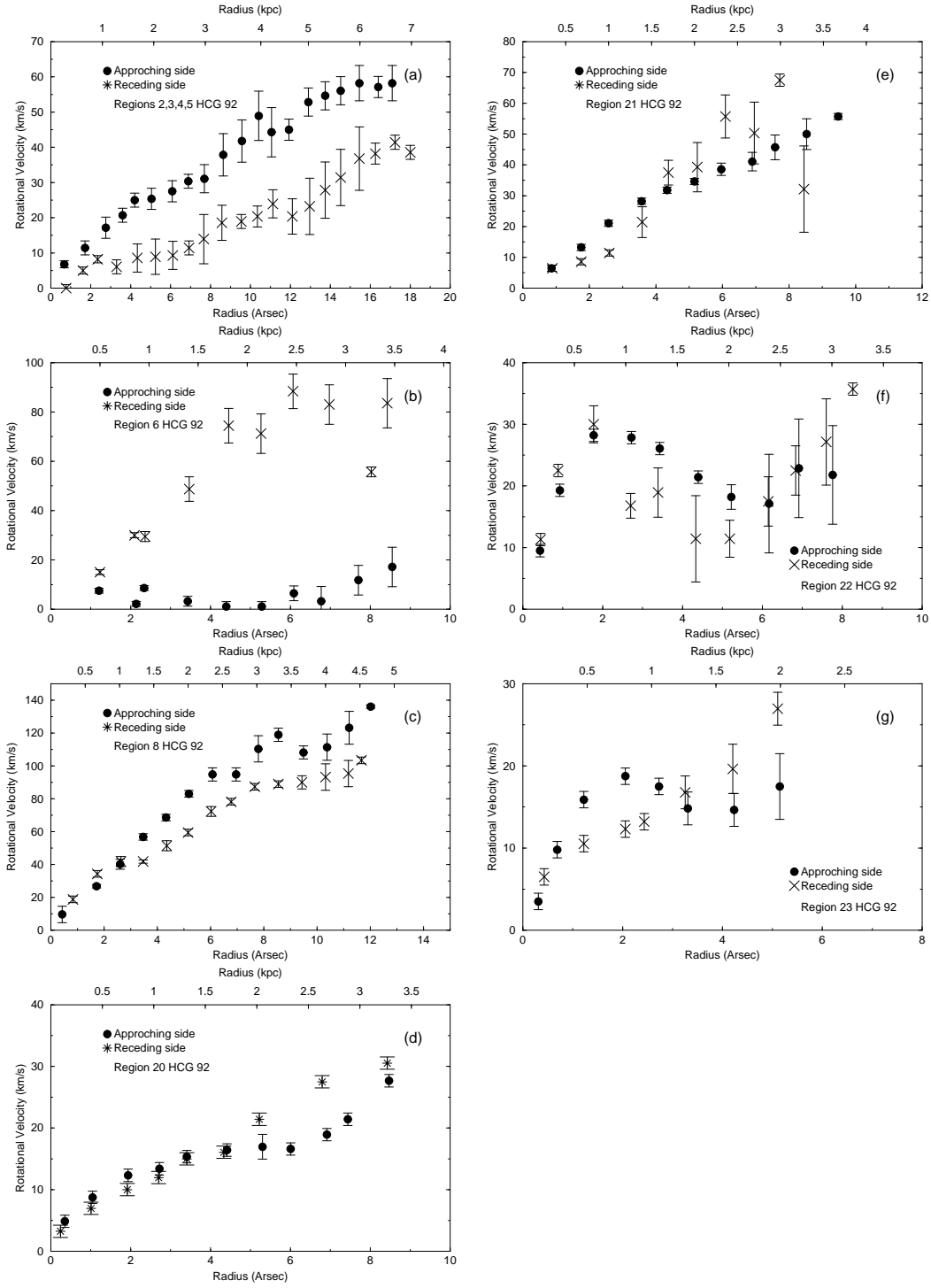


FIG. 4.— Rotation curves of the seven dwarf candidate galaxies. The parameters of the rotation curves are given in Table 3.

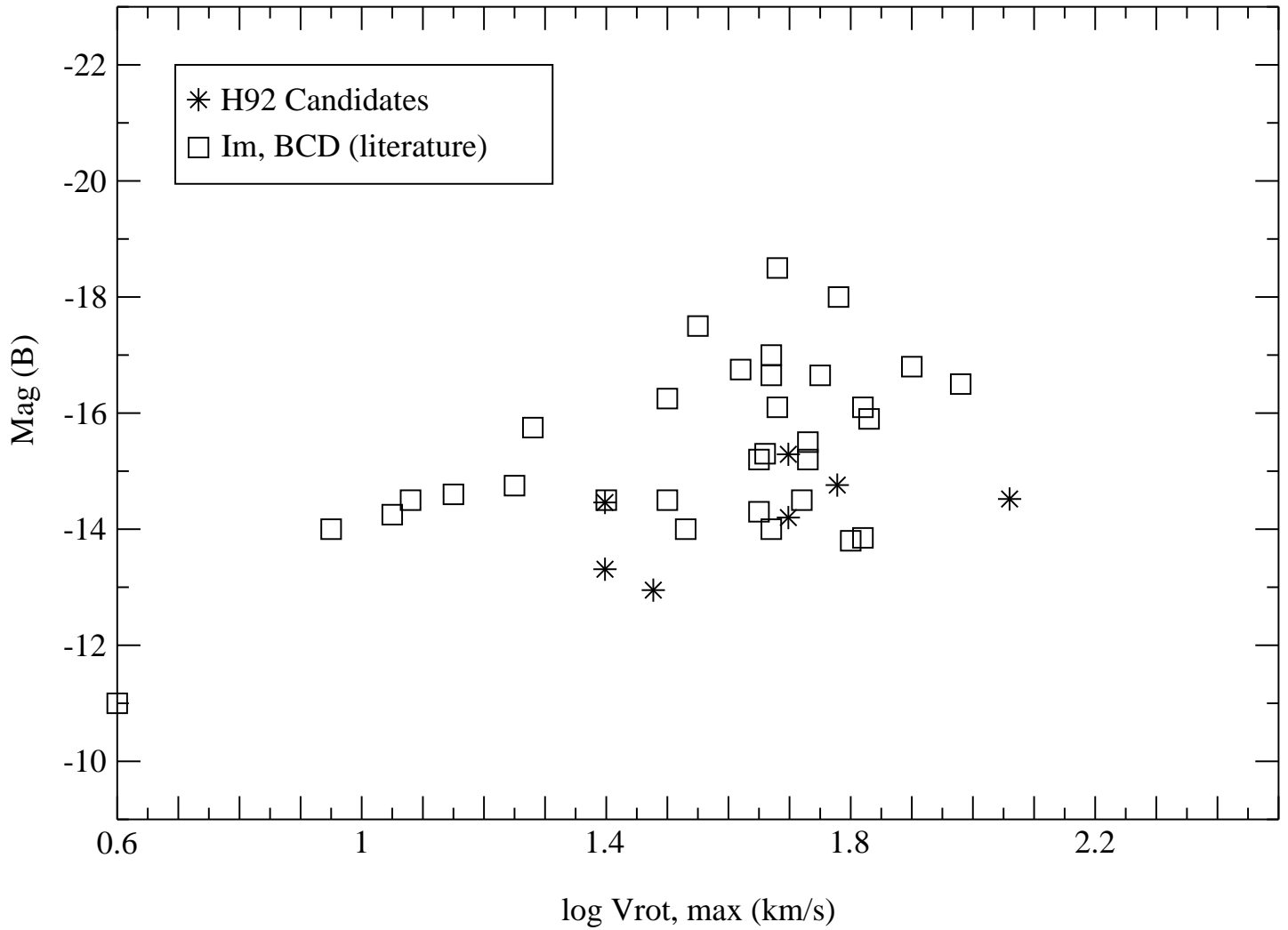


FIG. 5.— Plot showing the maximum rotation velocity (corrected for the inclination) versus the absolute B magnitude, for both the H92 tidal dwarf candidates and a compilation of Im and BCD galaxies from Hunter et al. 2000.

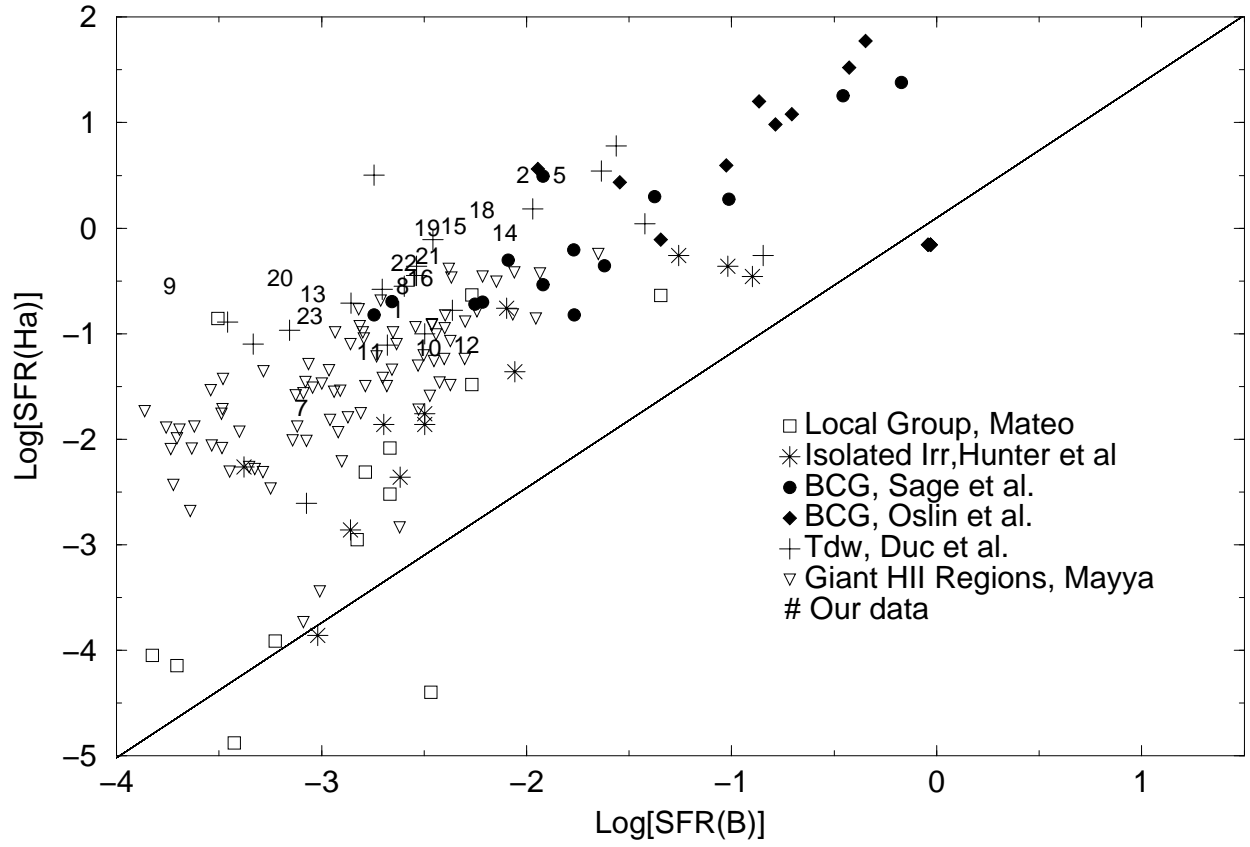


FIG. 6.— A plot of the current vs recent star formation rates for several different classes of emission line galaxies. The line corresponds to the locus where both measurements of the star-formation rates are equal.